

This is the accepted manuscript made available via CHORUS. The article has been published as:

Measurement of differential $t\bar{t}$ production cross sections in pp collisions

V. M. Abazov *et al.* (D0 Collaboration)

Phys. Rev. D **90**, 092006 — Published 19 November 2014

DOI: [10.1103/PhysRevD.90.092006](https://doi.org/10.1103/PhysRevD.90.092006)

Measurement of differential $t\bar{t}$ production cross sections in $p\bar{p}$ collisions

V.M. Abazov,³¹ B. Abbott,⁶⁷ B.S. Acharya,²⁵ M. Adams,⁴⁶ T. Adams,⁴⁴ J.P. Agnew,⁴¹ G.D. Alexeev,³¹ G. Alkhazov,³⁵ A. Alton^a,⁵⁶ A. Askew,⁴⁴ S. Atkins,⁵⁴ K. Augsten,⁷ C. Avila,⁵ F. Badaud,¹⁰ L. Bagby,⁴⁵ B. Baldin,⁴⁵ D.V. Bandurin,⁷³ S. Banerjee,²⁵ E. Barberis,⁵⁵ P. Baringer,⁵³ J.F. Bartlett,⁴⁵ U. Bassler,¹⁵ V. Bazterra,⁴⁶ A. Bean,⁵³ M. Begalli,² L. Bellantoni,⁴⁵ S.B. Beri,²³ G. Bernardi,¹⁴ R. Bernhard,¹⁹ I. Bertram,³⁹ M. Besançon,¹⁵ R. Beuselinck,⁴⁰ P.C. Bhat,⁴⁵ S. Bhatia,⁵⁸ V. Bhatnagar,²³ G. Blazey,⁴⁷ S. Blessing,⁴⁴ K. Bloom,⁵⁹ A. Boehnlein,⁴⁵ D. Boline,⁶⁴ E.E. Boos,³³ G. Borissov,³⁹ M. Borysova^l,³⁸ A. Brandt,⁷⁰ O. Brandt,²⁰ R. Brock,⁵⁷ A. Bross,⁴⁵ D. Brown,¹⁴ X.B. Bu,⁴⁵ M. Buehler,⁴⁵ V. Buescher,²¹ V. Bunichev,³³ S. Burdin^b,³⁹ C.P. Buszello,³⁷ E. Camacho-Pérez,²⁸ B.C.K. Casey,⁴⁵ H. Castilla-Valdez,²⁸ S. Caughron,⁵⁷ S. Chakrabarti,⁶⁴ K.M. Chan,⁵¹ A. Chandra,⁷² E. Chapon,¹⁵ G. Chen,⁵³ S.W. Cho,²⁷ S. Choi,²⁷ B. Choudhary,²⁴ S. Cihangir,⁴⁵ D. Claes,⁵⁹ J. Clutter,⁵³ M. Cooke^k,⁴⁵ W.E. Cooper,⁴⁵ M. Corcoran,⁷² F. Couderc,¹⁵ M.-C. Cousinou,¹² D. Cutts,⁶⁹ A. Das,⁴² G. Davies,⁴⁰ S.J. de Jong,^{29,30} E. De La Cruz-Burelo,²⁸ F. Déliot,¹⁵ R. Demina,⁶³ D. Denisov,⁴⁵ S.P. Denisov,³⁴ S. Desai,⁴⁵ C. Deterre^c,²⁰ K. DeVaughan,⁵⁹ H.T. Diehl,⁴⁵ M. Diesburg,⁴⁵ P.F. Ding,⁴¹ A. Dominguez,⁵⁹ A. Dubey,²⁴ L.V. Dudko,³³ A. Duperrin,¹² S. Dutt,²³ M. Eads,⁴⁷ D. Edmunds,⁵⁷ J. Ellison,⁴³ V.D. Elvira,⁴⁵ Y. Enari,¹⁴ H. Evans,⁴⁹ V.N. Evdokimov,³⁴ L. Feng,⁴⁷ T. Ferbel,⁶³ F. Fiedler,²¹ F. Filthaut,^{29,30} W. Fisher,⁵⁷ H.E. Fisk,⁴⁵ M. Fortner,⁴⁷ H. Fox,³⁹ S. Fuess,⁴⁵ P.H. Garbincius,⁴⁵ A. Garcia-Bellido,⁶³ J.A. García-González,²⁸ V. Gavrilov,³² W. Geng,^{12,57} C.E. Gerber,⁴⁶ Y. Gershtein,⁶⁰ G. Ginther,^{45,63} G. Golovanov,³¹ P.D. Grannis,⁶⁴ S. Greder,¹⁶ H. Greenlee,⁴⁵ G. Grenier,¹⁷ Ph. Gris,¹⁰ J.-F. Grivaz,¹³ A. Grohsjean^c,¹⁵ S. Grünendahl,⁴⁵ M.W. Grünewald,²⁶ T. Guillemin,¹³ G. Gutierrez,⁴⁵ P. Gutierrez,⁶⁷ J. Haley,⁶⁸ L. Han,⁴ K. Harder,⁴¹ A. Harel,⁶³ J.M. Hauptman,⁵² J. Hays,⁴⁰ T. Head,⁴¹ T. Hebbeker,¹⁸ D. Hedin,⁴⁷ H. Hegab,⁶⁸ A.P. Heinson,⁴³ U. Heintz,⁶⁹ C. Hensel,¹ I. Heredia-De La Cruz^d,²⁸ K. Herner,⁴⁵ G. Hesketh^f,⁴¹ M.D. Hildreth,⁵¹ R. Hirosky,⁷³ T. Hoang,⁴⁴ J.D. Hobbs,⁶⁴ B. Hoeneisen,⁹ J. Hogan,⁷² M. Hohlfeld,²¹ J.L. Holzbauer,⁵⁸ I. Howley,⁷⁰ Z. Hubacek,^{7,15} V. Hynek,⁷ I. Iashvili,⁶² Y. Ilchenko,⁷¹ R. Illingworth,⁴⁵ A.S. Ito,⁴⁵ S. Jabeen,⁶⁹ M. Jaffré,¹³ A. Jayasinghe,⁶⁷ M.S. Jeong,²⁷ R. Jesik,⁴⁰ P. Jiang,⁴ K. Johns,⁴² E. Johnson,⁵⁷ M. Johnson,⁴⁵ A. Jonckheere,⁴⁵ P. Jonsson,⁴⁰ J. Joshi,⁴³ A.W. Jung,⁴⁵ A. Juste,³⁶ E. Kajfasz,¹² D. Karmanov,³³ I. Katsanos,⁵⁹ R. Kehoe,⁷¹ S. Kermiche,¹² N. Khalatyan,⁴⁵ A. Khanov,⁶⁸ A. Kharchilava,⁶² Y.N. Kharzheev,³¹ I. Kiselevich,³² J.M. Kohli,²³ A.V. Kozelov,³⁴ J. Kraus,⁵⁸ A. Kumar,⁶² A. Kupco,⁸ T. Kurča,¹⁷ V.A. Kuzmin,³³ S. Lammers,⁴⁹ P. Lebrun,¹⁷ H.S. Lee,²⁷ S.W. Lee,⁵² W.M. Lee,⁴⁵ X. Lei,⁴² J. Lellouch,¹⁴ D. Li,¹⁴ H. Li,⁷³ L. Li,⁴³ Q.Z. Li,⁴⁵ J.K. Lim,²⁷ D. Lincoln,⁴⁵ J. Linnemann,⁵⁷ V.V. Lipaev,³⁴ R. Lipton,⁴⁵ H. Liu,⁷¹ Y. Liu,⁴ A. Lobodenko,³⁵ M. Lokajicek,⁸ R. Lopes de Sa,⁶⁴ R. Luna-Garcia^g,²⁸ A.L. Lyon,⁴⁵ A.K.A. Maciel,¹ R. Madar,¹⁹ R. Magaña-Villalba,²⁸ S. Malik,⁵⁹ V.L. Malyshev,³¹ J. Mansour,²⁰ J. Martínez-Ortega,²⁸ R. McCarthy,⁶⁴ C.L. McGivern,⁴¹ M.M. Meijer,^{29,30} D. Meister^m,⁴⁶ A. Melnitchouk,⁴⁵ D. Menezes,⁴⁷ P.G. Mercadante,³ M. Merkin,³³ A. Meyer,¹⁸ J. Meyerⁱ,²⁰ F. Miconi,¹⁶ N.K. Mondal,²⁵ M. Mulhearn,⁷³ E. Nagy,¹² M. Narain,⁶⁹ R. Nayyar,⁴² H.A. Neal,⁵⁶ J.P. Negret,⁵ P. Neustroev,³⁵ H.T. Nguyen,⁷³ T. Nunnemann,²² J. Orduna,⁷² N. Osman,¹² J. Osta,⁵¹ A. Pal,⁷⁰ N. Parashar,⁵⁰ V. Parihar,⁶⁹ S.K. Park,²⁷ R. Partridge^e,⁶⁹ N. Parua,⁴⁹ A. Patwa^j,⁶⁵ B. Penning,⁴⁵ M. Perfilov,³³ Y. Peters,⁴¹ K. Petridis,⁴¹ G. Petrillo,⁶³ P. Pétroff,¹³ M.-A. Pleier,⁶⁵ V.M. Podstavkov,⁴⁵ A.V. Popov,³⁴ M. Prewitt,⁷² D. Price,⁴¹ N. Prokopenko,³⁴ J. Qian,⁵⁶ A. Quadt,²⁰ B. Quinn,⁵⁸ P.N. Ratoff,³⁹ I. Razumov,³⁴ I. Ripp-Baudot,¹⁶ F. Rizatdinova,⁶⁸ M. Rominsky,⁴⁵ A. Ross,³⁹ C. Royon,¹⁵ P. Rubinov,⁴⁵ R. Ruchti,⁵¹ G. Sajot,¹¹ A. Sánchez-Hernández,²⁸ M.P. Sanders,²² A.S. Santos^h,¹ G. Savage,⁴⁵ L. Sawyer,⁵⁴ T. Scanlon,⁴⁰ R.D. Schamberger,⁶⁴ Y. Scheglov,³⁵ H. Schellman,⁴⁸ C. Schwanenberger,⁴¹ R. Schwienhorst,⁵⁷ J. Sekaric,⁵³ H. Severini,⁶⁷ E. Shabalina,²⁰ V. Shary,¹⁵ S. Shaw,⁵⁷ A.A. Shchukin,³⁴ V. Simak,⁷ P. Skubic,⁶⁷ P. Slatery,⁶³ D. Smirnov,⁵¹ G.R. Snow,⁵⁹ J. Snow,⁶⁶ S. Snyder,⁶⁵ S. Söldner-Rembold,⁴¹ L. Sonnenschein,¹⁸ K. Soustruznik,⁶ J. Stark,¹¹ D.A. Stoyanova,³⁴ M. Strauss,⁶⁷ L. Suter,⁴¹ P. Svoisky,⁶⁷ M. Titov,¹⁵ V.V. Tokmenin,³¹ Y.-T. Tsai,⁶³ D. Tsybychev,⁶⁴ B. Tuchming,¹⁵ C. Tully,⁶¹ L. Uvarov,³⁵ S. Uvarov,³⁵ S. Uzunyan,⁴⁷ R. Van Kooten,⁴⁹ W.M. van Leeuwen,²⁹ N. Varelas,⁴⁶ E.W. Varnes,⁴² I.A. Vasilyev,³⁴ A.Y. Verkheev,³¹ L.S. Vertogradov,³¹ M. Verzocchi,⁴⁵ M. Vesterinen,⁴¹ D. Vilanova,¹⁵ P. Vokac,⁷ H.D. Wahl,⁴⁴ M.H.L.S. Wang,⁴⁵ J. Warchol,⁵¹ G. Watts,⁷⁴ M. Wayne,⁵¹ J. Weichert,²¹ L. Welty-Rieger,⁴⁸ M.R.J. Williams,⁴⁹ G.W. Wilson,⁵³ M. Wobisch,⁵⁴ D.R. Wood,⁵⁵ T.R. Wyatt,⁴¹ Y. Xie,⁴⁵ R. Yamada,⁴⁵ S. Yang,⁴ T. Yasuda,⁴⁵ Y.A. Yatsunenko,³¹ W. Ye,⁶⁴ Z. Ye,⁴⁵ H. Yin,⁴⁵ K. Yip,⁶⁵ S.W. Youn,⁴⁵ J.M. Yu,⁵⁶ J. Zennaro,⁶² T.G. Zhao,⁴¹ B. Zhou,⁵⁶ J. Zhu,⁵⁶ M. Zielinski,⁶³ D. Zieminska,⁴⁹ and L. Zivkovic¹⁴

(The D0 Collaboration*)

- ¹LAFEX, Centro Brasileiro de Pesquisas Físicas, Rio de Janeiro, Brazil
- ²Universidade do Estado do Rio de Janeiro, Rio de Janeiro, Brazil
- ³Universidade Federal do ABC, Santo André, Brazil
- ⁴University of Science and Technology of China, Hefei, People's Republic of China
- ⁵Universidad de los Andes, Bogotá, Colombia
- ⁶Charles University, Faculty of Mathematics and Physics,
Center for Particle Physics, Prague, Czech Republic
- ⁷Czech Technical University in Prague, Prague, Czech Republic
- ⁸Institute of Physics, Academy of Sciences of the Czech Republic, Prague, Czech Republic
- ⁹Universidad San Francisco de Quito, Quito, Ecuador
- ¹⁰LPC, Université Blaise Pascal, CNRS/IN2P3, Clermont, France
- ¹¹LPSC, Université Joseph Fourier Grenoble 1, CNRS/IN2P3,
Institut National Polytechnique de Grenoble, Grenoble, France
- ¹²CPPM, Aix-Marseille Université, CNRS/IN2P3, Marseille, France
- ¹³LAL, Université Paris-Sud, CNRS/IN2P3, Orsay, France
- ¹⁴LPNHE, Universités Paris VI and VII, CNRS/IN2P3, Paris, France
- ¹⁵CEA, Irfu, SPP, Saclay, France
- ¹⁶IPHC, Université de Strasbourg, CNRS/IN2P3, Strasbourg, France
- ¹⁷IPNL, Université Lyon 1, CNRS/IN2P3, Villeurbanne, France and Université de Lyon, Lyon, France
- ¹⁸III. Physikalisches Institut A, RWTH Aachen University, Aachen, Germany
- ¹⁹Physikalisches Institut, Universität Freiburg, Freiburg, Germany
- ²⁰II. Physikalisches Institut, Georg-August-Universität Göttingen, Göttingen, Germany
- ²¹Institut für Physik, Universität Mainz, Mainz, Germany
- ²²Ludwig-Maximilians-Universität München, München, Germany
- ²³Panjab University, Chandigarh, India
- ²⁴Delhi University, Delhi, India
- ²⁵Tata Institute of Fundamental Research, Mumbai, India
- ²⁶University College Dublin, Dublin, Ireland
- ²⁷Korea Detector Laboratory, Korea University, Seoul, Korea
- ²⁸CINVESTAV, Mexico City, Mexico
- ²⁹Nikhef, Science Park, Amsterdam, the Netherlands
- ³⁰Radboud University Nijmegen, Nijmegen, the Netherlands
- ³¹Joint Institute for Nuclear Research, Dubna, Russia
- ³²Institute for Theoretical and Experimental Physics, Moscow, Russia
- ³³Moscow State University, Moscow, Russia
- ³⁴Institute for High Energy Physics, Protvino, Russia
- ³⁵Petersburg Nuclear Physics Institute, St. Petersburg, Russia
- ³⁶Institució Catalana de Recerca i Estudis Avançats (ICREA) and Institut de Física d'Altes Energies (IFAE), Barcelona, Spain
- ³⁷Uppsala University, Uppsala, Sweden
- ³⁸Taras Shevchenko National University of Kyiv, Kiev, Ukraine
- ³⁹Lancaster University, Lancaster LA1 4YB, United Kingdom
- ⁴⁰Imperial College London, London SW7 2AZ, United Kingdom
- ⁴¹The University of Manchester, Manchester M13 9PL, United Kingdom
- ⁴²University of Arizona, Tucson, Arizona 85721, USA
- ⁴³University of California Riverside, Riverside, California 92521, USA
- ⁴⁴Florida State University, Tallahassee, Florida 32306, USA
- ⁴⁵Fermi National Accelerator Laboratory, Batavia, Illinois 60510, USA
- ⁴⁶University of Illinois at Chicago, Chicago, Illinois 60607, USA
- ⁴⁷Northern Illinois University, DeKalb, Illinois 60115, USA
- ⁴⁸Northwestern University, Evanston, Illinois 60208, USA
- ⁴⁹Indiana University, Bloomington, Indiana 47405, USA
- ⁵⁰Purdue University Calumet, Hammond, Indiana 46323, USA
- ⁵¹University of Notre Dame, Notre Dame, Indiana 46556, USA
- ⁵²Iowa State University, Ames, Iowa 50011, USA
- ⁵³University of Kansas, Lawrence, Kansas 66045, USA
- ⁵⁴Louisiana Tech University, Ruston, Louisiana 71272, USA
- ⁵⁵Northeastern University, Boston, Massachusetts 02115, USA
- ⁵⁶University of Michigan, Ann Arbor, Michigan 48109, USA
- ⁵⁷Michigan State University, East Lansing, Michigan 48824, USA
- ⁵⁸University of Mississippi, University, Mississippi 38677, USA
- ⁵⁹University of Nebraska, Lincoln, Nebraska 68588, USA
- ⁶⁰Rutgers University, Piscataway, New Jersey 08855, USA
- ⁶¹Princeton University, Princeton, New Jersey 08544, USA
- ⁶²State University of New York, Buffalo, New York 14260, USA

⁶³University of Rochester, Rochester, New York 14627, USA
⁶⁴State University of New York, Stony Brook, New York 11794, USA
⁶⁵Brookhaven National Laboratory, Upton, New York 11973, USA
⁶⁶Langston University, Langston, Oklahoma 73050, USA
⁶⁷University of Oklahoma, Norman, Oklahoma 73019, USA
⁶⁸Oklahoma State University, Stillwater, Oklahoma 74078, USA
⁶⁹Brown University, Providence, Rhode Island 02912, USA
⁷⁰University of Texas, Arlington, Texas 76019, USA
⁷¹Southern Methodist University, Dallas, Texas 75275, USA
⁷²Rice University, Houston, Texas 77005, USA
⁷³University of Virginia, Charlottesville, Virginia 22904, USA
⁷⁴University of Washington, Seattle, Washington 98195, USA

The production of top quark-antiquark pair events in $p\bar{p}$ collisions at $\sqrt{s} = 1.96$ TeV is studied as a function of the transverse momentum and absolute value of the rapidity of the top quarks as well as of the invariant mass of the $t\bar{t}$ pair. We select events containing an isolated lepton, a large imbalance in transverse momentum, and four or more jets with at least one jet identified as originating from a b quark. The data sample corresponds to 9.7 fb^{-1} of integrated luminosity recorded with the D0 detector during Run II of the Fermilab Tevatron Collider. Observed differential cross sections are consistent with standard model predictions.

PACS numbers: 14.65.Ha, 12.38.Qk, 13.85.Qk

I. INTRODUCTION

The top quark, discovered by the CDF and D0 experiments in 1995 [1, 2], is the heaviest of all elementary particles in the standard model (SM), with a mass of $173.2 \pm 0.9 \text{ GeV}$ [3]. The production of top quark-antiquark pairs ($t\bar{t}$) at the Fermilab Tevatron Collider is dominated by the quark-antiquark ($q\bar{q}$) annihilation process. The measurement of $t\bar{t}$ differential production cross sections provides a direct test of quantum chromodynamics (QCD), the theory of the strong interactions. Moreover, a precise modeling of QCD processes is vital in many searches for contributions from new phenomena, where differential top quark cross sections can be used to set constraints on new sources of physics. A detailed understanding of top quark production is also needed for measurements or searches where new particles decay to a $t\bar{t}$ pair, where other particles are produced in association with a $t\bar{t}$ pair, or where $t\bar{t}$ production is among the dominant backgrounds. An example of the importance of accurate modeling of QCD is given by the deviation observed in the charge asymmetry measurement in $p\bar{p} \rightarrow t\bar{t}$ production from SM predictions [4–7]. Such

a difference could be due to the exchange of a new heavy mediator, e.g., an axigluon [8, 9] that could also enhance the $t\bar{t}$ cross section. Differential cross sections, most notably the one as a function of the invariant mass of the $t\bar{t}$ pair $d\sigma/dm(t\bar{t})$, provide stringent constraints on axigluon models [10]. Differential $t\bar{t}$ production cross sections have been previously measured both at the Tevatron [10, 11] and the LHC [12, 13]. The earlier measurements of differential $t\bar{t}$ production at the Tevatron as a function of the transverse momentum of the t and \bar{t} quark (p_T^{top}) [11], and as a function of $m(t\bar{t})$ [10], showed good agreement with perturbative QCD (pQCD) calculations at next-to-leading (NLO), as well as next-to-next-to-leading order (NNLO) [14]. Compared to the previous D0 result [11], the current measurement employs a factor of ten more data allowing for higher precision tests of pQCD.

Single differential cross sections are measured as a function of $m(t\bar{t})$, the absolute value of the rapidity¹ $|y^{\text{top}}|$, and p_T^{top} , using events with a topology consistent with $t\bar{t}$ decays. The index “top” in $|y^{\text{top}}|$ and p_T^{top} refers to either t or \bar{t} quarks. The observed t and \bar{t} differential distributions are consistent with each other, hence they are combined. Events are selected in the lepton+jets decay channel, where the lepton (ℓ) refers to either an electron or a muon. This channel corresponds to $t\bar{t} \rightarrow W^+bW^-\bar{b}$ decays, where one of the two W bosons decays leptonically ($W \rightarrow \ell\nu$), and the other hadronically ($W \rightarrow q\bar{q}'$). This decay channel includes also small

*with visitors from ^aAugustana College, Sioux Falls, SD, USA, ^bThe University of Liverpool, Liverpool, UK, ^cDESY, Hamburg, Germany, ^dUniversidad Michoacana de San Nicolas de Hidalgo, Morelia, Mexico ^eSLAC, Menlo Park, CA, USA, ^fUniversity College London, London, UK, ^gCentro de Investigacion en Computacion - IPN, Mexico City, Mexico, ^hUniversidade Estadual Paulista, São Paulo, Brazil, ⁱKarlsruher Institut für Technologie (KIT) - Steinbuch Centre for Computing (SCC), D-76128 Karlsruhe, Germany, ^jOffice of Science, U.S. Department of Energy, Washington, D.C. 20585, USA, ^kAmerican Association for the Advancement of Science, Washington, D.C. 20005, USA and ^lKiev Institute for Nuclear Research, Kiev, Ukraine ^mETH Zürich, Zürich, Switzerland

¹ The rapidity y is defined as $y = 1/2 \cdot \ln[(E + p_z)/(E - p_z)]$, where E is the energy of a particle and p_z is the z -component of its momentum vector \vec{p} . The direction of the z -axis is defined along the proton beam direction.

contributions from electrons and muons stemming from the decay of τ leptons ($t \rightarrow Wb \rightarrow \tau\nu_\tau b \rightarrow \ell\nu_\ell\nu_\tau b$). The events are required to contain, in addition to the lepton, at least four jets and an imbalance in transverse momentum \cancel{E}_T , as discussed in section IV.

II. MONTE CARLO SIMULATIONS AND QCD PREDICTIONS

Monte Carlo (MC) simulations are used to model the reconstruction of the observables, to estimate systematic uncertainties associated with the measurements, and to simulate physics processes. Different MC event generators are used to implement hard scattering processes based on leading-order (LO) and NLO QCD calculations, and are complemented with parton shower evolution. To simulate detector effects, generated events (including hadronization) are passed through a detailed simulation of the D0 detector response based on GEANT3 [15]. To account for effects from additional overlapping $p\bar{p}$ interactions, events without any trigger requirements are selected randomly in collider data and overlaid on the fully simulated MC events.

The $t\bar{t}$ samples are generated with MC@NLO version 3.4 [16], which includes the production of off-shell top quarks by taking into account their finite width or with ALPGEN version 2.11 [17], which produces only on-shell top quarks. Single top quark production ($q\bar{q}' \rightarrow t\bar{b}, q'g \rightarrow tq\bar{b}$) is modeled using COMPHEP [18]. For events generated with MC@NLO, the parton showering is performed with HERWIG version 6.510 [19], whereas for ALPGEN and COMPHEP parton showering is implemented by PYTHIA version 6.409 [20]. In the following the term “scale” and the symbol μ refer to the renormalization and factorization scales, which are assumed to be equal and evaluated for the specific processes. The parton density functions (PDF), and other choices made in generating simulated events are summarized in Table I. For all the MC simulations involving the generation of top quarks a top quark mass of $m_t = 172.5$ GeV is used. The difference from the current Tevatron top quark mass measurement of 173.2 GeV [3] has negligible impact on the analysis and is treated as a systematic uncertainty (see Sec. IX).

Several QCD predictions for differential $t\bar{t}$ cross sections have been calculated at higher orders than those included in the MC generators. They use approximate NNLO calculations based on next-to-next-to-leading logarithm (NNLL) resummation for $m_t = 173$ GeV to calculate the p_T^{top} and $|y^{\text{top}}|$ differential distributions [14, 23], and $m_t = 172.5$ GeV to calculate the $m(t\bar{t})$ and p_T^{top} differential distributions [24]. All use the MSTW2008NNLO PDF [25]. The scale used to calculate the p_T^{top} and $|y^{\text{top}}|$ differential distributions is m_t . Employing m_t as the scale for calculating the $m(t\bar{t})$ distribution leads to large and negative NLO corrections that result in negative differential cross sections at approximate NNLO, especially at large $m(t\bar{t})$. In Ref. [24],

TABLE I: Details of the signal and background modeling employed in this measurement. All final-state particles are used to compute the chosen scale, except the decay products of the W boson, and are consequently used to calculate the mass m and p_T . The term m_V refers to the mass of the W or Z boson. The CTEQ6L1 [21] and CTEQ6M [22] PDFs are used.

Process	Generator	Scale, μ	PDF
$t\bar{t}$	ALPGEN	$\sqrt{\sum(m^2 + p_T^2)}$	CTEQ6L1
$t\bar{t}$	MC@NLO	$\sqrt{\sum(m^2 + p_T^2)}$	CTEQ6M
W +jets	ALPGEN	$\sqrt{m_V^2 + \sum(m^2 + p_T^2)}$	CTEQ6L1
Z/γ^* +jets	ALPGEN	$\sqrt{m_V^2 + \sum(m^2 + p_T^2)}$	CTEQ6L1
Diboson	PYTHIA	$\sqrt{m_V^2 + \sum(m^2 + p_T^2)}$	CTEQ6L1
single top (s -channel)	COMPHEP	m_t	CTEQ6L1
single top (t -channel)	COMPHEP	$m_t/2$	CTEQ6M

the $m(t\bar{t})$ distribution is calculated using the scale $m(t\bar{t})$ instead, which avoids this issue, but leads to a 7.7% lower inclusive cross section.

When comparing to D0 data, we normalize the total cross section of the calculations in Ref. [24] for the p_T^{top} and $m(t\bar{t})$ distributions to match the inclusive fully resummed NNLL at NNLO QCD calculation (using $m_t = 172.5$ GeV and the MSTW2008NNLO PDF), which finds $\sigma_{\text{tot}}^{\text{res}} = 7.35_{-0.27}^{+0.23}$ (scale + pdf) pb [26]. The total cross section of the approximate NNLO calculation as in Ref. [14, 23] is calculated from the p_T^{top} distribution and yields $7.08_{-0.24}^{+0.20}$ (scale) $_{-0.27}^{+0.36}$ (PDF) pb. The inclusive cross section calculated by integrating the $|y^{\text{top}}|$ or p_T^{top} distribution deviates by 1.1%. For reasons of consistency, the p_T^{top} and $|y^{\text{top}}|$ distributions from Refs. [14, 23] are not re-scaled from their original predictions.

A. Backgrounds

The main background to $t\bar{t}$ in the ℓ +jets final state is W +jets production. It consists of events where one W boson is produced via an electroweak interaction, together with additional partons from QCD processes. The W +jets final state can be split into four subsamples according to parton flavor: $Wb\bar{b}$ +jets, $Wc\bar{c}$ +jets, Wc +jets and W +light jets, where light refers to gluons, u , d or s quarks. The LO ALPGEN cross sections are corrected for NLO effects as provided by MCFM [27]: the W +jets cross section is multiplied by 1.30, and the $Wb\bar{b}$ +jets and $Wc\bar{c}$ +jets (Wc +jets) cross sections are multiplied by an additional 1.5 (1.3). The p_T distribution of the W boson in MC simulation is reweighted to match the product of the p_T distribution of the Z boson measured in D0 data [28] and the SM ratio of these two distributions, which was calculated at NLO using RESBOS [29].

Other backgrounds include events from Z/γ^* +jets production, which include Z bosons decaying to electron,

muon or tau pairs. The LO ALPGEN predictions are similarly corrected using the NLO calculation of MCFM. The $Z/\gamma^* + \text{jets}$ cross section is multiplied by 1.3, and the $Zc\bar{c} + \text{jets}$ and $Zb\bar{b} + \text{jets}$ cross sections by an additional 1.7 and 1.5, respectively. The simulated p_T distribution of the Z boson is reweighted to match the measured p_T distribution in $Z \rightarrow \ell\ell$ [28].

The single top quark background consists of s - and t -channel single top quark production, which are normalized to the NLO cross sections of 1.04 and 2.26 pb [30], respectively. As the single top quark background yields only a few events passing all selection criteria described later, no effects are considered from the dependence of this background on m_t .

Diboson production (WW , WZ and ZZ bosons) processes are normalized to NLO cross sections, calculated with MCFM, of 11.6 pb, 3.3 pb and 1.3 pb, respectively.

III. THE D0 DETECTOR

The D0 detector [31] consists of several subdetectors designed for identification and reconstruction of the products of $p\bar{p}$ collisions. A silicon microstrip tracker (SMT) [32, 33] and central fiber tracker surround the interaction region for pseudorapidities² $|\eta| < 3$ and $|\eta| < 2.5$, respectively. These elements of the central tracking system are located within a superconducting solenoidal magnet generating a 1.9 T field, providing measurements for reconstructing event vertices and trajectories of charged particles. The SMT allows for a precision of 40 μm or better for the reconstructed primary $p\bar{p}$ interaction vertex (PV) in the plane transverse to the beam direction. The impact parameter of typical charged particle trajectories relative to the PV is determined with a precision between 20 and 50 μm depending on the number of SMT hits and particle momenta. The impact parameter and its measurement uncertainty are key components of lifetime-based identification of jets containing b quarks [34]. Particle energies are measured using a liquid argon sampling calorimeter that is segmented into a central calorimeter covering $|\eta| < 1.1$, and two end calorimeters extending the coverage to $|\eta| = 4.2$. Outside of the calorimetry, trajectories of muons are measured using three layers of tracking detectors and scintillation trigger counters, and an iron toroidal magnet generating a 1.8 T field between the first two layers. Plastic scintillator arrays are located in front of the end-calorimeter cryostats to measure the luminosity [35].

² The pseudorapidity $\eta = -\ln[\tan(\theta/2)]$ is measured relative to the center of the detector, and θ is the polar angle with respect to the proton beam direction.

IV. EVENT SELECTION

This analysis uses all the data recorded by the D0 detector at $\sqrt{s} = 1.96$ TeV. After applying data quality requirements, the data corresponds to an integrated luminosity of 9.7 fb⁻¹. The trigger selects $\ell + \text{jets}$ events by requiring at least one lepton (electron or muon) with an efficiency of 95% or 80% for $t\bar{t}$ events containing an electron or muon candidate, respectively.

Accepted events must have a reconstructed PV within 60 cm of the center of the detector along the beam axis, one lepton with transverse momentum $p_T > 20$ GeV and $|\eta| < 1.1$ (for electrons) or $|\eta| < 2$ (for muons), and $\cancel{E}_T > 20$ GeV. The measurement of \cancel{E}_T is based on calorimetry. In addition, leptons are required to originate from the PV by demanding $|\Delta z(\ell, \text{PV})| < 1$ cm. A distance $\Delta R = \sqrt{\Delta\eta^2 + \Delta\phi^2}$ between a lepton and a jet of $\Delta R(\ell, \text{closest jet}) > 0.5$ is required to ensure that leptons are isolated [36, 37]. For the $\mu + \text{jets}$ sample upper limits on the transverse mass of the reconstructed W boson of $M_T^W < 250$ GeV and $\cancel{E}_T < 250$ GeV are applied to remove events in data with misreconstructed muon p_T . To further remove such events, we employ an additional requirement on the significance of the track curvature \mathcal{S}_c , which is defined as the ratio of the curvature, κ , and the expected uncertainty on κ measured for the track associated with the muon. We employ two selection requirements with different slopes in the azimuthal ($\Delta\phi$) vs. \mathcal{S}_c plane: $(-70 + 25.47 \cdot \Delta\phi(\mu, \cancel{E}_T)) < |\mathcal{S}_c|$ and $(-8.76 + 4.38 \cdot \Delta\phi(\mu, \cancel{E}_T)) < |\mathcal{S}_c|$. Figure 1(a) shows these requirements indicated by the solid lines in the $|\mathcal{S}_c|$ versus $\Delta\phi(\mu, \cancel{E}_T)$ plane for $t\bar{t}$ events and (b) for $W + \text{jets}$ background events. The cut on \mathcal{S}_c removes low momentum muons misreconstructed at high momenta whilst keeping 97% of the leptons stemming from $t\bar{t}$ decays. A minimum separation in azimuth of $\Delta\phi(\ell, \cancel{E}_T) > 0.5$ is imposed between the direction of the lepton and the direction of the missing momentum, to reduce multijet background caused by the misidentification of a jet as a lepton and the consequent impact on the accompanying \cancel{E}_T . Further reduction of the multijet background is achieved by requiring an additional minimum separation in azimuth between the isolated lepton and \cancel{E}_T : $\Delta\phi(e, \cancel{E}_T) > 2.2 - 0.045 \cdot \cancel{E}_T/\text{GeV}$ and $\Delta\phi(\mu, \cancel{E}_T) > 2.1 - 0.035 \cdot \cancel{E}_T/\text{GeV}$. After correcting the energy of the jet to the particle level [38] at least four jets with $p_T > 20$ GeV and $|\eta| < 2.5$ are required. The jet with highest p_T is also required to have $p_T > 40$ GeV.

Due to the high instantaneous luminosity provided by the Tevatron, additional $p\bar{p}$ collisions may occur within the same bunch crossing. As noted above, events from randomly selected beam crossings with the same instantaneous luminosity are overlaid on the simulated events, which are reweighted to match the luminosity profile observed in data. To suppress jets from these additional collisions, jets are required to contain two tracks consistent with originating from the PV. At least one of the jets must be selected as

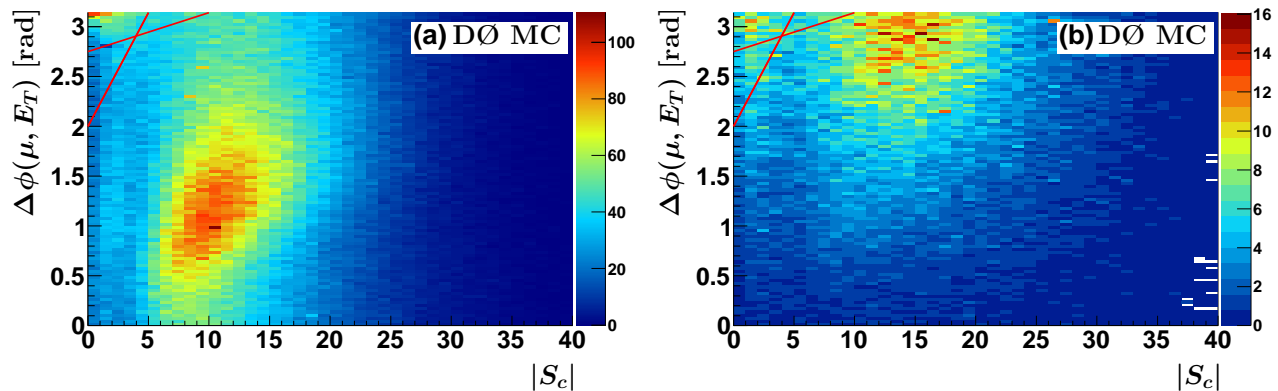


FIG. 1: (color online) The $|S_c|$ versus $\Delta\phi(\mu, \cancel{E}_T)$ plane for (a) $t\bar{t}$ events and (b) for W +jets background events. The selection requirements are indicated by the solid lines.

likely to originate from a b quark (b tagged) using a multivariate discriminant (MVD) [34]. The discriminant combines variables that characterize the presence and properties of secondary vertices and tracks within jets. The MVD identification of jets containing b quarks has an efficiency of approximately 60%, with a light quark misidentification rate of approximately 1.2%. Events containing more than one isolated muon or electron, which satisfy the lepton requirements discussed above, are rejected.

V. SAMPLE COMPOSITION

Background contributions are categorized into instrumental background and irreducible background from processes with final states similar to $t\bar{t}$. Instrumental background is due to multijet processes where a jet is misidentified as an electron in the e +jets channel, or with a muon originating from the semileptonic decay of a heavy hadron appears to be isolated in the μ +jets channel. Data-driven [39, 40] and MC simulation methods are employed to model the instrumental background. The irreducible background processes are estimated using MC simulations described in Sec. II. Most of this background arises from W +jets production, and to constrain it we use the $\ell + 2$ jets and $\ell + 3$ jets data (dominated by W +jets production) in addition to the $\ell + \geq 4$ jets sample (dominated by $t\bar{t}$ production). We determine the sample composition from a simultaneous fit for the $t\bar{t}$ cross section and the heavy-flavor contribution originating from W +jets. The fit is made to the MVD b identification output distribution; Fig. 2 shows the distribution after applying the fit results for the $\ell + 2$ jets, $\ell + 3$ jets and $\ell + \geq 4$ jets data sample in the (a) e +jets and (b) μ +jets decay channel. The simultaneous fit yields a W +jets heavy-flavor scale factor $s_{\text{fit}}^{\text{WHF}} = 0.89 \pm 0.08$ to be applied to the $Wb\bar{b}$ + jets and $Wc\bar{c}$ + jets contributions in addition to the factors

discussed in Sec. II. Similar procedures were used in previous measurements by D0 [40]. The simultaneous fit to the $\ell + 2$ jets, $\ell + 3$ jets and $\ell + \geq 4$ jets samples yields a $t\bar{t}$ cross section of $\sigma_{\text{fit}}^{t\bar{t}} = 8.00 \pm 0.40$ (stat.) pb. We verified that there is no need for an additional scale factor to accommodate the Z/γ^* +jets heavy-flavor contributions $s_{\text{fit}}^{\text{ZHF}}$ by using a modified version of the simultaneous fit taking into account $s_{\text{fit}}^{\text{ZHF}}$ instead of $s_{\text{fit}}^{\text{WHF}}$. The $\sigma_{\text{fit}}^{t\bar{t}}$ serves as an initial value of the $t\bar{t}$ cross section in the $t\bar{t}$ differential cross section measurement using inclusive four-jet data.

The total inclusive $t\bar{t}$ cross section is also calculated using only events with at least four jets from the three differential distributions by integrating all bins of each of the cross section distributions, as presented below in Sec. VIII and average the resulting three inclusive cross sections as discussed in Sec. X. This yields a compatible value of $\sigma(p\bar{p} \rightarrow t\bar{t}) = 8.0 \pm 0.7$ (stat.) ± 0.8 (syst.) pb. The $t\bar{t}$ contributions in the following plots are derived employing MC@NLO simulated events normalized to this measured inclusive $t\bar{t}$ cross section of 8.0 pb.

Figures 3 and 4 demonstrate, respectively, the quality of the modeling of the selected events in the e +jets and μ +jets sample with the background and signal contributions. The signal contribution is derived employing MC@NLO simulated events normalized to the measured inclusive $t\bar{t}$ cross section of 8.0 pb. The expected composition of the sample after the final selection is given in Table II.

VI. EXTRACTION OF THE SIGNAL

To reconstruct the four-vectors of the full $t\bar{t}$ decay chain, $t\bar{t} \rightarrow W^+b + W^-\bar{b} \rightarrow (q\bar{q}')b + (\ell\nu)\bar{b}$, we use a constrained kinematic reconstruction algorithm [46] that takes into account experimental resolutions. In total the algorithm uses 18 parameters based on the measurements of jets, leptons and \cancel{E}_T . The masses of the W boson and

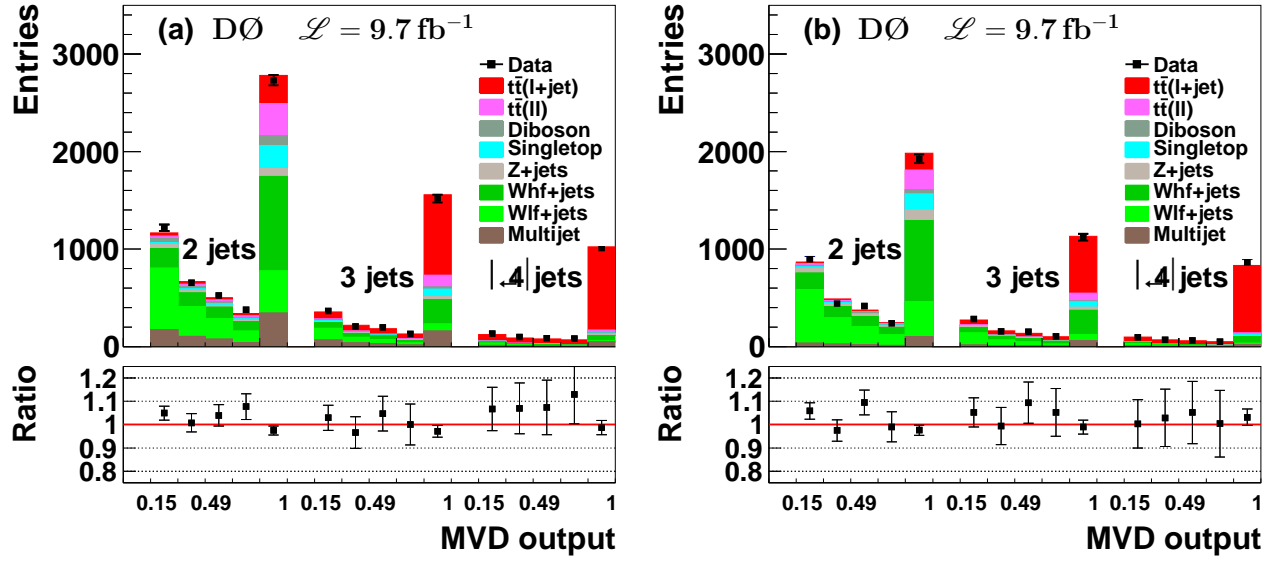


FIG. 2: (color online) Distributions of the MVD b identification output distribution for the $\ell + 2$ jets, $\ell + 3$ jets and $\ell + \geq 4$ jets data sample in the (a) e +jets and (b) μ +jets decay channel. The data are compared to the sum of predicted contributions from signal and background processes. More details on how the sample composition is derived can be found in the text.

TABLE II: Expected number of events with at least four jets due to each process (uncertainties are statistical and systematic added in quadrature). The sample composition is determined as discussed in Section V. Events in the $t\bar{t}$ dilepton decay channel are denoted by $\ell\ell$.

Process	μ +jets	e +jets
Multijet	31.1 ± 10.0	75.1 ± 56.3
W +jets	164.9 ± 15.9	148.8 ± 14.3
Diboson	9.1 ± 0.8	10.5 ± 0.9
Z/γ^* +jets	11.9 ± 1.2	12.4 ± 1.5
Single top	16.1 ± 2.2	21.8 ± 3.0
$t\bar{t}, \ell\ell$	22.6 ± 2.0	33.5 ± 2.9
\sum bgs	254.4 ± 19.1	302.1 ± 58.3
$t\bar{t}, \ell$ +jets	838.7 ± 72.5	1088.7 ± 94.2
\sum (sig + bgs)	1093.1 ± 75.0	1390.8 ± 110.8
Data	1137	1403

the t quark are fixed to 80.4 GeV and 172.5 GeV, respectively. The \cancel{E}_T provides the initial estimate for the p_T of the neutrino. The longitudinal momentum $p_z(\nu)$ is estimated by constraining the mass of the W boson decay products to 80.4 GeV. This yields a quadratic equation in $p_z(\nu)$ with two solutions. These solutions, together with the 12 possible jet-quark assignments yield 24 possible solutions to the kinematic reconstruction algorithm. The large number of solutions is reduced by assigning b -tagged jets to b quarks. The solution with the best χ^2 for assigning the reconstructed objects to the parton-level quantities serves as the input to the unfolding (see Sec. VII). This solution corresponds to the correct assign-

ment of the jets to the quarks from the $t\bar{t}$ decay in MC events in 80% of the cases. The observed and expected distributions in χ^2 are compared in Fig. 5.

The modeling of signal and background processes is verified through a comparison of the data to the number of expected $t\bar{t}$ signal events and the sum of all background contributions. The expected $t\bar{t}$ contribution is derived employing MC@NLO simulated events normalized to the measured inclusive cross section of 8.0 pb. Figures 6–8 show the reconstructed $m(t\bar{t})$, $|y^{\text{top}}|$, and p_T^{top} distributions before unfolding. The $|y^{\text{top}}|$ and p_T^{top} distributions include both $W \rightarrow \ell\nu$ and $W \rightarrow q\bar{q}'$ decay modes (two entries per event). The resolutions in the two decay modes are similar, hence they are combined. The distributions in (a) of Figs. 6–8 show the data compared to the $t\bar{t}$ signal and background processes, while (b) shows the background-subtracted data. The data and its description by the sum of signal and background processes agree within uncertainties.

VII. MEASUREMENT TECHNIQUE

Measurements involving top quarks benefit from the very short lifetime of the t quark, since it decays before it can hadronize. Effects of hadronization and QCD corrections are thus reduced. Moreover, at Tevatron energies the transverse momentum of $t\bar{t}$ pairs is almost always smaller than $m(t\bar{t})$ and production is central, so that almost the entire phase space of $t\bar{t}$ production is within the detector acceptance. Corrections to measured quantities as well as their uncertainties are therefore small, leading to well measured top-quark cross sections.

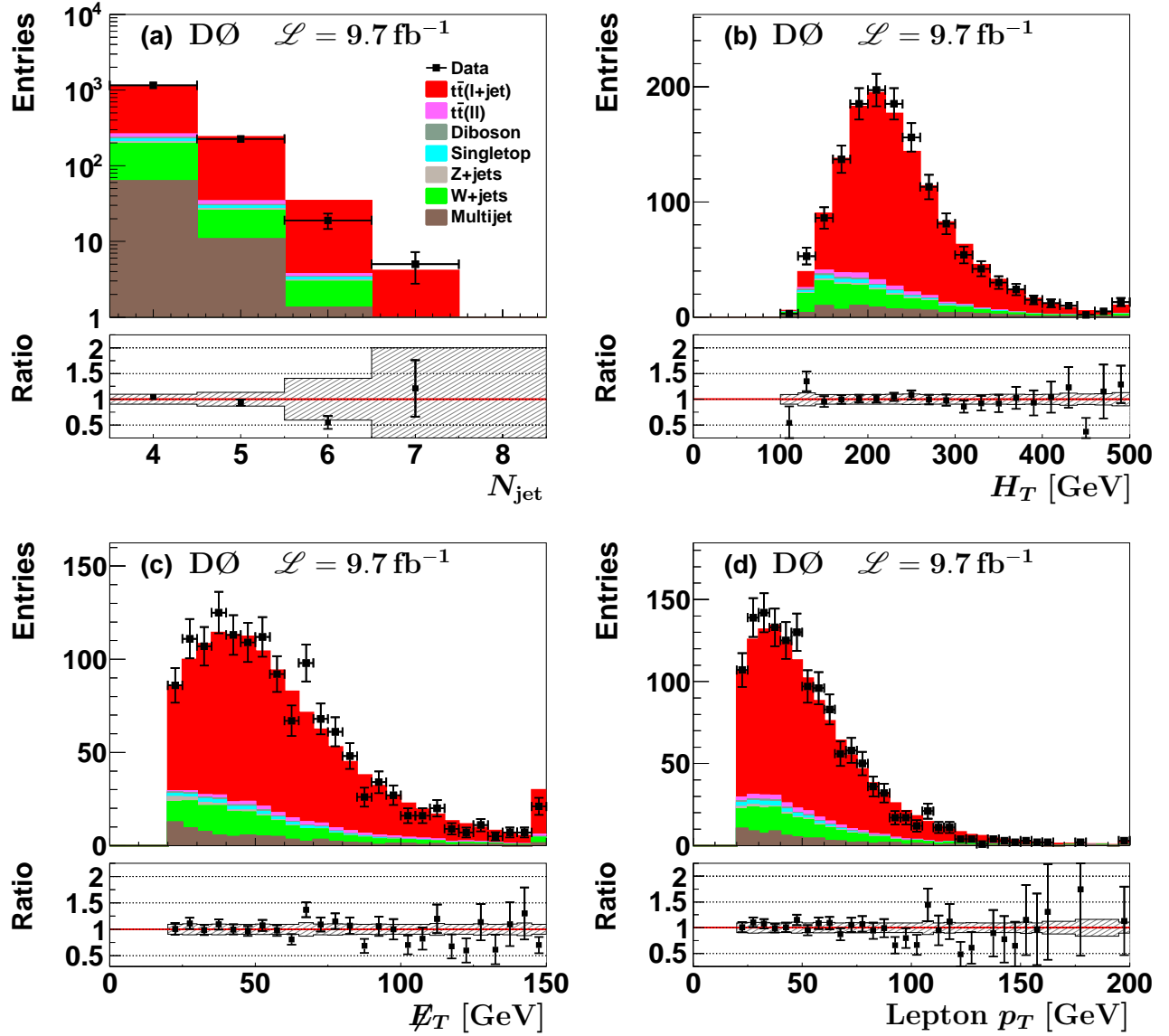


FIG. 3: (color online) Distributions of (a) the number of jets, (b) the scalar sum of the p_T values of the lepton and jets, (c) E_T , and (d) lepton p_T for the e +jets final state. The data are compared to the sum of predicted contributions from signal and background processes. The signal contribution is derived employing MC@NLO simulated events normalized to the measured inclusive $t\bar{t}$ cross section of 8.0 pb. The highest bin in the histograms is used as an overflow bin. The ratios of data to the sum of the signal and all background contributions are shown in the panels below the distributions. The bands show the 1 s.d. combined systematic uncertainties on the sum of the signal and background contributions.

The differential cross-sections are defined for parton-level top quarks including off-shell effects and are corrected for detector and QCD effects using a regularized matrix unfolding procedure [41, 42]. This procedure reduces the influence of model dependencies in the cross section determination and introduces correlations among the bins used in the measurement. These correlations are minimized by regularization. Unfolding event migrations relies on a migration matrix (A), which describes the relation between the generated distribution of a vari-

able (\vec{x}_{gen}) and its reconstructed distribution (\vec{y}_{rec}) as $A\vec{x}_{\text{gen}} = \vec{y}_{\text{rec}}$. Each matrix element A_{ij} is the probability for an event originating from bin j of \vec{x}_{gen} to be measured in bin i of \vec{y}_{rec} . The migration matrix is based on the simulation of the D0 detector. The reconstruction-level bins used in the migration matrix are twice as narrow as the generator level bins, in order to provide detailed information on the bin-to-bin migrations, and improve the accuracy of the unfolding [43]. The generated distribution \vec{x}_{gen} can be estimated using A^\dagger , the pseudoinverse [44] of the matrix A : $\vec{x}_{\text{gen}} = A^\dagger \vec{y}_{\text{rec}}$. As with ordinary

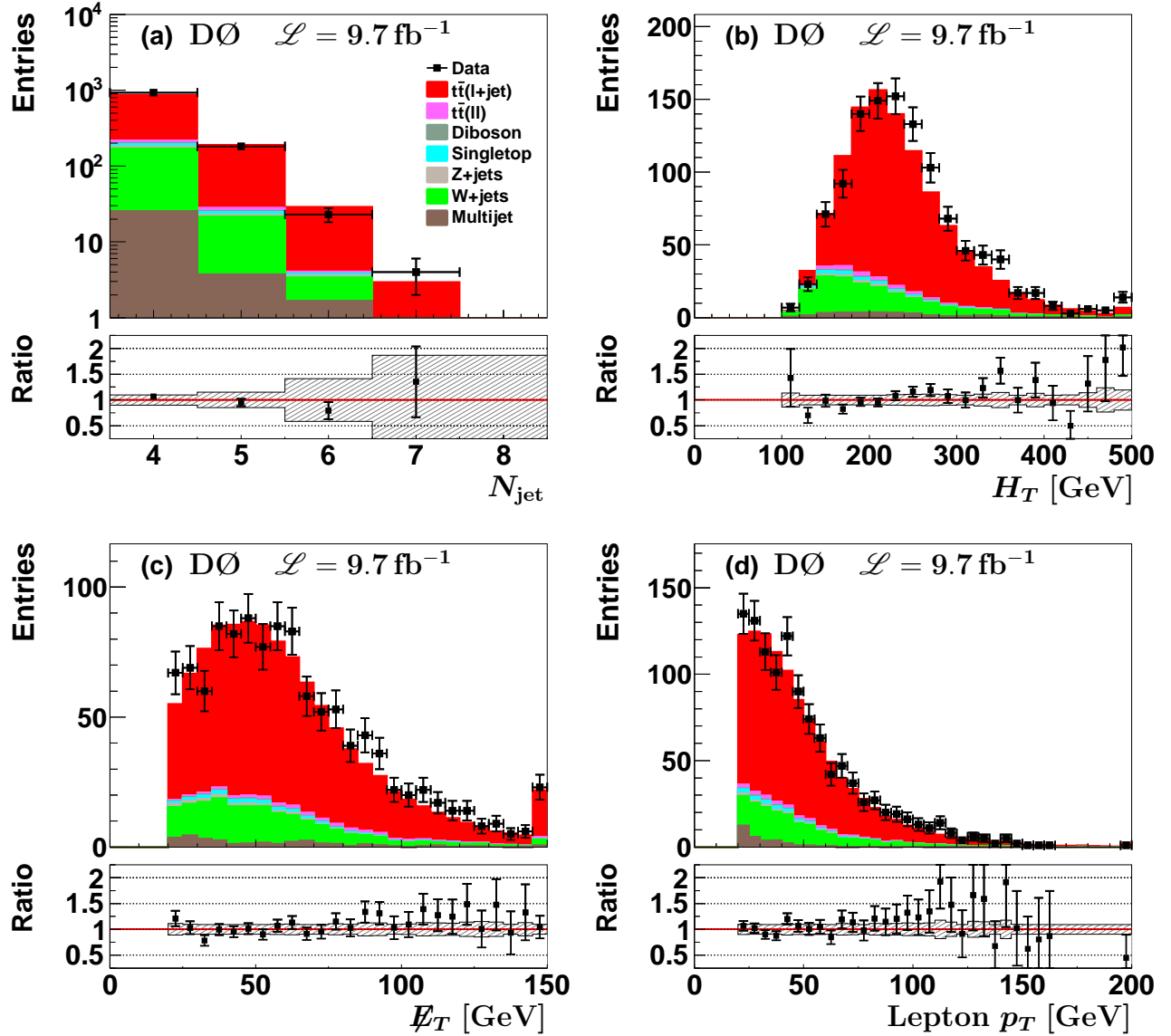


FIG. 4: (color online) Distributions of (a) the number of jets, (b) the scalar sum of the p_T values of the lepton and jets, (c) E_T , and (d) lepton p_T for the μ +jets final state. The data are compared to the sum of predicted contributions from signal and background processes. The signal contribution is derived employing MC@NLO simulated events normalized to the measured inclusive $t\bar{t}$ cross section of 8.0 pb. The highest bin in the histograms is used as an overflow bin. The ratios of data to the sum of the signal and all background contributions are shown in the panels below the distributions. The bands show the 1 s.d. combined systematic uncertainties on the sum of the signal and background contributions.

matrix inversion, this results in large contributions that lack statistical significance. Such contributions can be minimized by imposing regularization, which leads to an effective cutoff of the insignificant terms. We employ regularized unfolding as implemented in the TUNFOLD package [45]. The regularization is based on the derivative of the distribution and is done in twice as many bins as are used in the final results. An insufficient regularization admits fluctuations into the unfolded result, whereas excessive regularization overly biases the measurement towards the MC generated distribution. The value of the

regularization strength is determined using the so-called L-curve approach [45] that balances the consistency of the unfolded data x with the initial data y against the scatter of x . The scatter of x can be caused by fluctuations in cases in which an insufficient regularization is chosen. A χ^2 statistic measures the tension between x , the data and the scatter of x . Within the earlier mentioned bounds, a systematic uncertainty is derived for this procedure as discussed in Sect. IX E. The statistical uncertainties of the differential measurements are computed analytically with TUNFOLD and verified using an

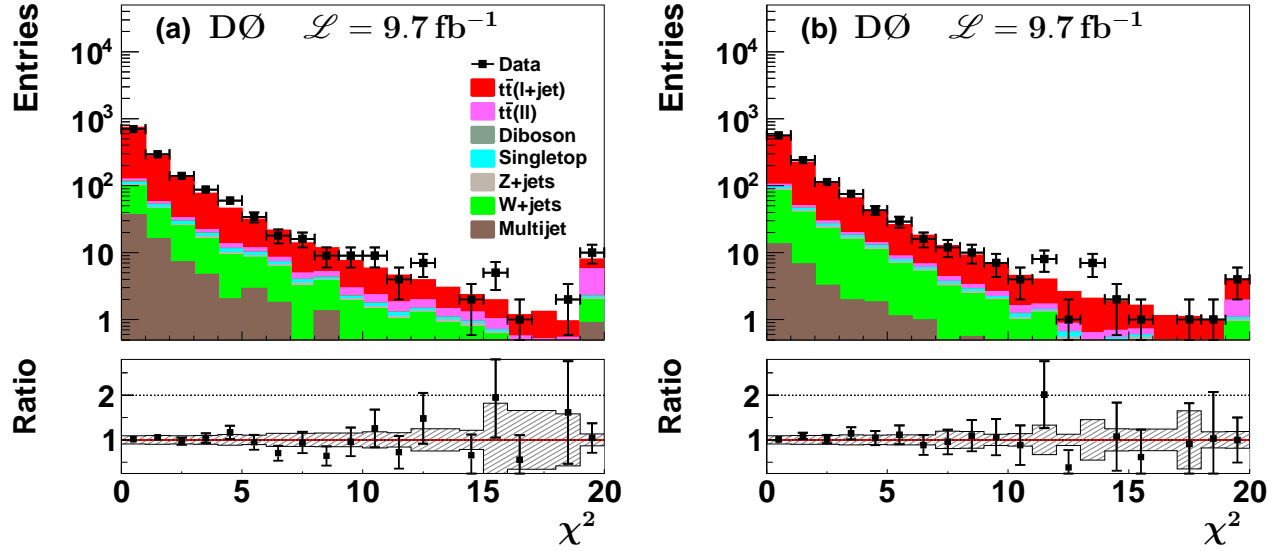


FIG. 5: (color online) Distribution of χ^2 for the best solution with lowest χ^2 for the (a) e +jets and (b) μ +jets final states. The data are compared to the sum of predicted contributions from signal and background processes. The signal contribution is derived employing MC@NLO simulated events normalized to the measured inclusive $t\bar{t}$ cross section of 8.0 pb. The highest bin in the histograms is used as an overflow bin. The ratios of data to the sum of the signal and all background contributions are shown in the panels below the distributions. The bands show the 1 s.d. combined systematic uncertainties on the sum of the signal and background contributions.

ensemble of simulated pseudo-datasets. The covariance matrix is calculated by propagating the uncertainties of the reconstructed distribution \vec{y}_{rec} through the unfolding process.

VIII. CROSS SECTION DETERMINATION

Equation 1 is used to calculate the differential $t\bar{t}$ cross section σ_i as a function of the observable X , where i denotes an individual bin, and ΔX_i its width.

$$\frac{d\sigma_i}{dX} = \frac{N_i^{\text{unfold}}}{\mathcal{L} \cdot B \cdot \Delta X_i} . \quad (1)$$

The unfolded number of signal events N_i^{unfold} is corrected for the branching fraction B into the ℓ +jets decay channel of 0.342 ± 0.02 [47] and used to obtain the cross section for the total integrated luminosity \mathcal{L} that corresponds to the selection requirements, including data quality cuts. The branching fraction used in Eq. 1 includes electrons and muons originating from the decay of τ leptons. The number of expected background events is estimated through MC simulations and data-driven methods and is subtracted from data to determine N_i^{unfold} . The numbers of background-subtracted events are corrected for effects due to limited detector resolution and efficiency by means of the regularized matrix unfolding as discussed in Sec. VII. By using this procedure, the

IX. SYSTEMATIC UNCERTAINTIES

Systematic uncertainties are assessed by varying the values of a specific parameter used in the modeling of the data, and repeating the analysis. Unless otherwise stated, the magnitude of the parameter modifications is obtained from alternative calibrations of the MC simulation. The migration matrix and the background contributions are extracted from these different MC models, while the regularization strength is fixed to that for the nominal unfolded data. The difference between the nominal unfolded data and unfolded data, including a modification due to a specific parameter serves as the estimate of an individual source of systematic uncertainty. Individual sources of systematic uncertainty are added in quadrature for each bin of a differential cross section. The largest uncertainties usually arise at large values of $m(t\bar{t})$, $|y^{\text{top}}|$, or p_T^{top} , where there are fewer events. Table III summarizes the systematic uncertainties on the inclusive and differential cross sections. Numbers stated in the column denoted with $|\delta_{\text{diff}}|$ illustrate the size of the systematic uncertainties in individual bins of the differential measurements.

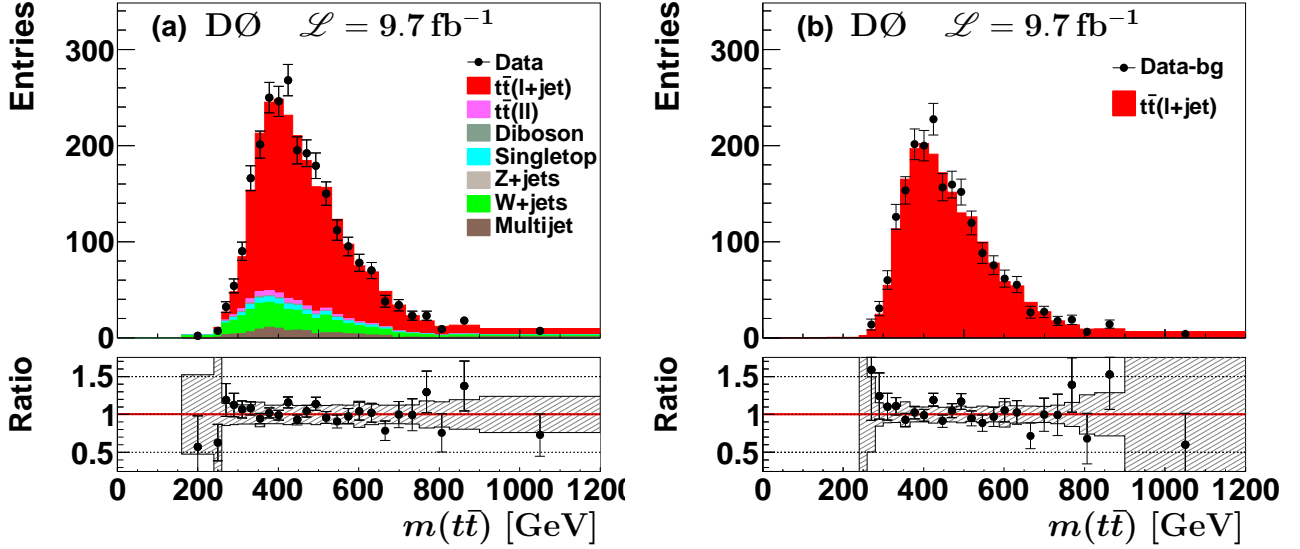


FIG. 6: (color online) Distribution of $m(t\bar{t})$, (a) compared to the sum of predicted contributions from signal and background processes, and (b) the background-subtracted distribution. The signal contribution is derived employing MC@NLO simulated events normalized to the measured inclusive $t\bar{t}$ cross section of 8.0 pb. The lower panels indicate the ratio of the data to (a) the sum of the signal and all background processes, and (b) to the signal process only.

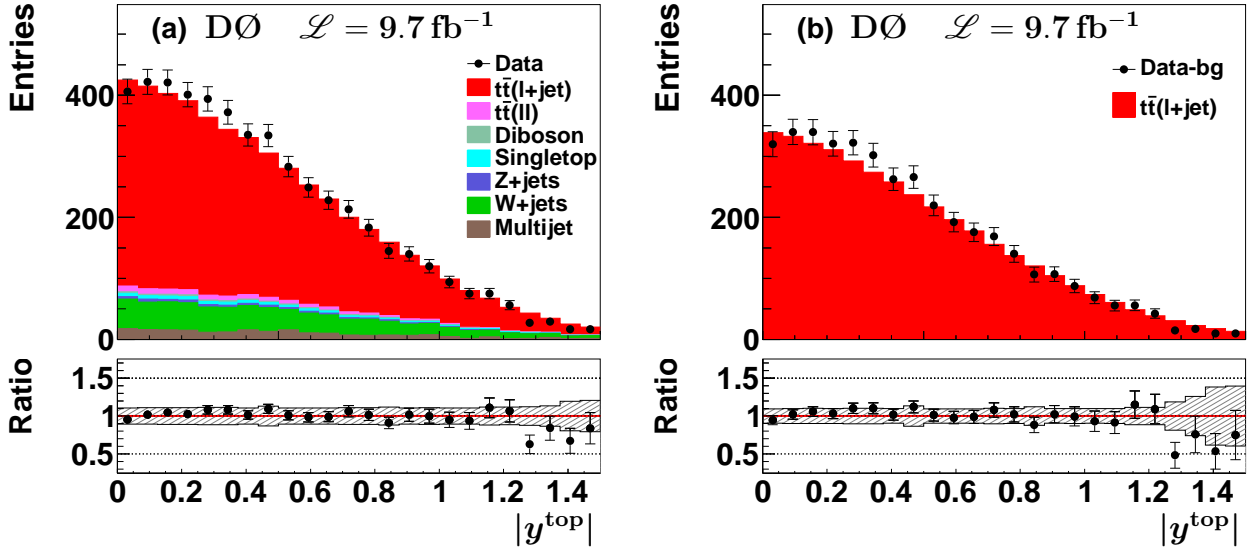


FIG. 7: (color online) Distribution of $|y^{\text{top}}|$, (a) compared to the sum of predicted contributions from signal and background processes, and (b) the background-subtracted distribution. The signal contribution is derived employing MC@NLO simulated events normalized to the measured inclusive $t\bar{t}$ cross section of 8.0 pb. The lower panels indicate the ratio of the data to (a) the sum of the signal and all background processes, and (b) to the signal process only.

A. Modeling of signal

The effect of NLO corrections on the matrix element for $t\bar{t}$ production is estimated by comparing $t\bar{t}$ events generated with MC@NLO+HERWIG to

those from ALPGEN+PYTHIA. From a comparison of ALPGEN+PYTHIA to ALPGEN+HERWIG, we find that the effect of hadronization uncertainties are less than those from the inclusion of higher-order effects. The top mass is varied within its uncertainty of ± 1 GeV [3]. An additional uncertainty on the signal arises from the relatively

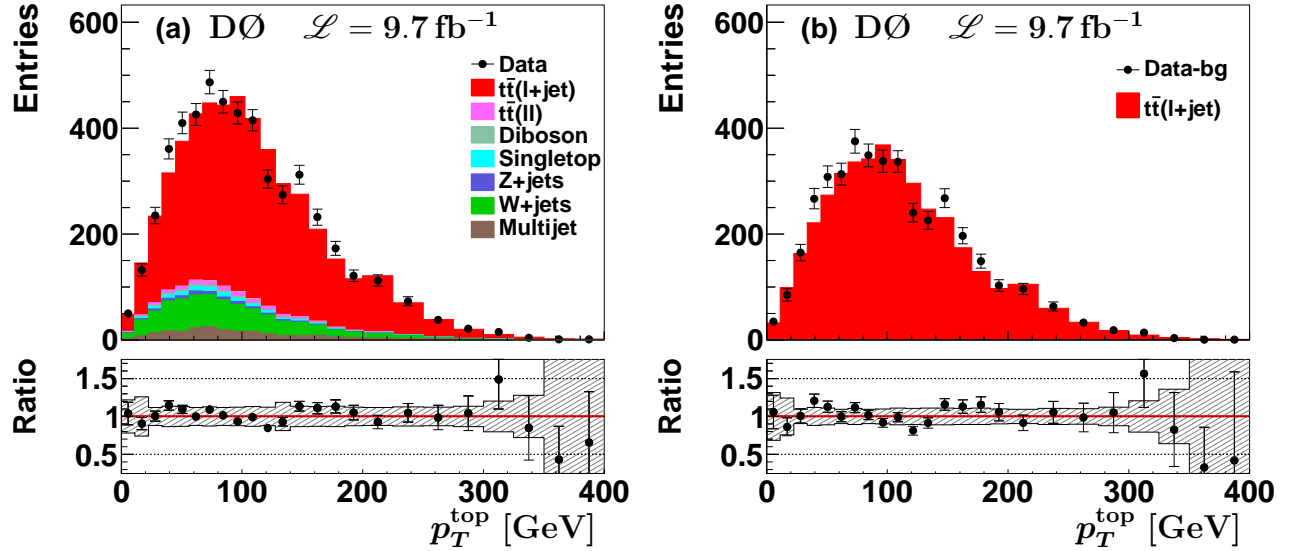


FIG. 8: (color online) Distribution of p_T^{top} , (a) compared to the sum of predicted contributions from signal and background processes, and (b) the background-subtracted distribution. The signal contribution is derived employing MC@NLO simulated events normalized to the measured inclusive $t\bar{t}$ cross section of 8.0 pb. The lower panels indicate the ratio of the data to (a) the sum of the signal and all background processes, and (b) to the signal process only.

TABLE III: Sources of systematic uncertainties. The uncertainty from each source on the inclusive cross section is given in the second columns. Systematic uncertainties in the binned values of the differential cross sections vary within the range given in the last column.

Source of uncertainty	Uncertainties, %	
	δ_{incl}	$ \delta_{\text{diff}} $
Signal modeling	+5.2/-4.4	4.0 – 14.2
PDF	+3.0/-3.4	0.9 – 4.4
Detector Modeling	+4.0/-4.1	3.1 – 13.7
Sample composition	± 1.8	2.8 – 9.2
Regularization strength	± 0.2	0.8 – 2.1
Integrated luminosity	± 6.1	6.1 – 6.1
Total systematic uncertainty	+9.6/-9.3	8.5 – 23.1

poor modeling of the reconstructed transverse momentum of the $t\bar{t}$ pair $p_T^{t\bar{t}}$ at D0 [4]. A systematic uncertainty is estimated by reweighting the distribution of the reconstructed $p_T^{t\bar{t}}$ in the MC simulation to the one observed in D0 data.

B. Parton distributions functions

The uncertainty on the cross sections due to the uncertainty on PDFs is estimated following the procedure of Ref. [22] by reweighting the MC simulation according to each of the 20 pairs of error eigenvectors of the CTEQ6M

PDF, with their effects added in quadrature.

C. Modeling of detector

Uncertainties on the modeling of the detector include uncertainties on trigger efficiency, lepton identification and b -quark identification. The uncertainty on trigger efficiency is roughly 2.5% for harder collisions ($p_T^{\text{top}} > 90$ GeV or $m(t\bar{t}) > 500$ GeV) and 6% for softer collisions that are typically closer to trigger thresholds. The p_T^{top} and $m(t\bar{t})$ differential cross-sections are modified according to these uncertainties, and the $|y^{\text{top}}|$ differential cross section is rederived with trigger efficiencies reweighted according to p_T^{top} . The identification efficiencies for b , c , light quarks (u, d, s) and gluons in MC simulations are calibrated using dijet data [48], and variations within the calibration uncertainty are used to determine the systematic uncertainty due to b -quark identification. Additional uncertainties arise from track multiplicity requirements on the selected jets in the identification of b quarks.

Other instrumental uncertainties from modeling the detector arise from the calibration of the jet energy, resolution and efficiency. The jet energy scale (JES) corrects the measured energy of the jet to the energy of its constituent particles. The JES is derived using a quark-jet dominated $\gamma + \text{jet}$ sample, and corrects for the difference in detector response between data and simulation. An additional correction based on single particle response ac-

counts for the different characteristics of quark and gluon jets. Jets in MC simulations have their transverse momenta smeared so that the simulated resolution matches the one observed in data. Calibrations to the jet reconstruction and identification efficiency in MC simulations are determined using $Z/\gamma^* + \text{jets}$ data. As mentioned earlier, jets are required to contain at least two tracks (see Section IV), and in MC simulations the corresponding efficiency is adjusted to match the one derived in dijet data. The uncertainties on the calibration of the jet energies, resolutions, and efficiencies as well as on the single particle response corrections are propagated to determine their effect on the differential cross sections.

D. Sample composition

Uncertainties on the composition of the selected events arise from the heavy-flavor scale factor used for $W + \text{jets}$ events, the assumed $t\bar{t}$ cross section, single top quark and diboson cross sections, and the estimate of the contributions from misidentified leptons. As described in Sec. V, the heavy-flavor scale factor in $W + \text{jets}$ and the assumed $t\bar{t}$ cross section are obtained from a simultaneous fit to the MVD distribution in the $\ell + 2\text{jets}$, $\ell + 3\text{jets}$ and $\ell + \geq 4\text{jets}$ samples. From the fit we derive a systematic uncertainty of 8% on the normalization of the $Wc\bar{c} + \text{jets}$ and $Wb\bar{b} + \text{jets}$ processes, and 5% on the normalization of the $t\bar{t}$ processes. The uncertainty on the single top quark cross sections is 12.6%, taken from varying the scale by factors of 2 and 0.5. An uncertainty of 7% on the diboson cross sections is assigned to the NLO predictions based on scale variation and PDF uncertainties. The uncertainties on the data-driven method of estimating multijet (MJ) background and its kinematic dependencies, mostly due to the uncertainties on the selection rates of true and false lepton candidates, are 75% in the $\mu + \text{jets}$ and 32% in the $e + \text{jets}$ sample. These uncertainties are estimated by varying the contribution of $Wc\bar{c} + \text{jets}$, $Wb\bar{b} + \text{jets}$, $Zc\bar{c} + \text{jets}$ and $Zb\bar{b} + \text{jets}$ by $\pm 20\%$, the $t\bar{t}$ contribution by $\pm 10\%$, comparing the fake and true signal rates in different variables (quoting the largest difference as additional parametrization uncertainty). In addition, to estimate the contribution of the fake rate uncertainty, a different \cancel{E}_T cut of < 15 GeV (standard cut for the fake rate estimation is < 10 GeV) [49] is applied. An overall 6.1% uncertainty on the luminosity [35] is assigned to the measured cross sections and is fully correlated across all bins of the differential cross section.

E. Regularization strength

As a procedural uncertainty in the unfolding method, the regularization strength is changed to higher and lower values by amounts consistent with the general bounds discussed in Sec. VII, and its impact is added to the total uncertainty. We test for a potential bias

by doing a closure test employing an ensemble of simulated pseudo-datasets, and find biases smaller than the assigned systematic uncertainty due to the unfolding procedure.

X. CROSS SECTIONS

The inclusive $t\bar{t}$ production cross section in the $\ell + \text{jets}$ decay channel can be calculated from any of the three differential measurements. We calculate it from the average of the three differential measurements in events with ≥ 4 jets weighted by the χ^2 as provided by the regularized unfolding (see Sec. VII), and we find:

$$\sigma^{t\bar{t}} = 8.0 \pm 0.7 (\text{stat.}) \pm 0.6 (\text{syst.}) \pm 0.5 (\text{lumi.}) \text{ pb.} \quad (2)$$

The inclusive $t\bar{t}$ production cross sections using the individual differential cross sections in $d\sigma/dp_T^{\text{top}}$, $|y^{\text{top}}|$ and $m(t\bar{t})$ are $8.0 \pm 1.1 (\text{tot.})$ pb, $8.2 \pm 1.1 (\text{tot.})$ pb and $7.8 \pm 1.0 (\text{tot.})$ pb, respectively. The differences between these results have been verified to be statistically consistent using ensemble tests including correlations between the three measurements. These results are in agreement with the inclusive result of Sec. V, which was based on the inclusive $\ell + 2\text{jets}$ sample. The inclusive $t\bar{t}$ production cross section (Eq. (2)) is in agreement with the inclusive fully resummed NNLL at NNLO QCD calculation (see Sec. II), which gives $\sigma_{\text{tot}}^{\text{res}} = 7.35_{-0.27}^{+0.23} (\text{scale} + \text{pdf})$ pb. The total cross section of the approximate NNLO calculation as in Ref. [14, 23] is calculated from the p_T^{top} distribution and yields $7.08_{-0.24}^{+0.20} (\text{scale})_{-0.27}^{+0.36} (\text{PDF})$ pb. The data may also be compared to differential cross section predictions from MC@NLO and ALPGEN, that correspond to total cross sections of $\sigma_{\text{tot}} = 7.54$ pb and $\sigma_{\text{tot}} = 5.61$ pb, respectively.

The fully corrected differential cross sections are shown in Figs. 9–11, for $m(t\bar{t})$, $|y^{\text{top}}|$, and p_T^{top} , respectively. The corresponding correlation coefficients of the differential measurements are presented in Table IV to VI in Appendix A. For p_T^{top} and $|y^{\text{top}}|$ distributions we present the average t and \bar{t} cross sections. The differential cross sections are listed in Table VII to IX in Appendix A. Note that the correlated normalization uncertainty on the differential data points is about $\pm 6.6\%$, dominated by the uncertainty on the measurement of the integrated luminosity. For quantitative comparison to SM predictions, the covariance matrices (Tables X–XII) for the results are presented in Appendix A. No bin centering correction is applied to the measurements, and the cross sections are displayed at the center of each bin. Contributions beyond the highest bin boundary are included in the last bin of the $m(t\bar{t})$, $|y^{\text{top}}|$, and p_T^{top} distributions. As shown in Fig. 6, there are no contributions to the differential cross section for $m(t\bar{t})$ below 240 GeV.

Figure 9(a) shows the cross section for the unfolded data as a function of $m(t\bar{t})$ and (b) shows the ratio of

the cross section and several predictions to the approximate NNLO distribution [24]. Within the systematic uncertainties the MC@NLO and approximate NNLO describe the data, while the ALPGEN prediction is low in absolute normalization as shown in Fig. 9(b). The distribution for $|y^{\text{top}}|$ is shown in Fig. 10. The ratio in Fig. 10(b) indicates that the distribution predicted by QCD at approximate NNLO is in marginal agreement with the data for $|y^{\text{top}}|$. The predictions by MC@NLO describe the data better. As shown in Fig. 11(a), the differential cross section as a function of p_T^{top} is reasonably described by MC@NLO and the approximate NNLO QCD prediction. The MC@NLO prediction describes the shape of the p_T^{top} distribution well.

This new result is consistent with an earlier measurement by D0 using 1.0 fb^{-1} of data [11]. Statistical uncertainties are defined differently in Ref. [11], following Ref. [50], and are not directly comparable with the current uncertainties. The statistical uncertainties reported here are computed analytically and verified using an ensemble of simulated pseudo-datasets. Results presented here supersede the results of Ref. [11].

XI. CONCLUSIONS

Differential cross sections for $t\bar{t}$ production have been measured in the ℓ +jets decay channels using the full Tevatron data set at $\sqrt{s} = 1.96 \text{ TeV}$. The data are corrected for detector efficiency, acceptance and bin migration by means of a regularized unfolding procedure. The differential cross sections are measured with a typical precision of 9% as a function of the invariant mass of the $t\bar{t}$ system $m(t\bar{t})$, the absolute rapidity of the t and \bar{t} quarks $|y^{\text{top}}|$, and the transverse momentum p_T^{top} . The measured differential cross sections are in general agreement with predictions by QCD generators and predictions at approximate NNLO.

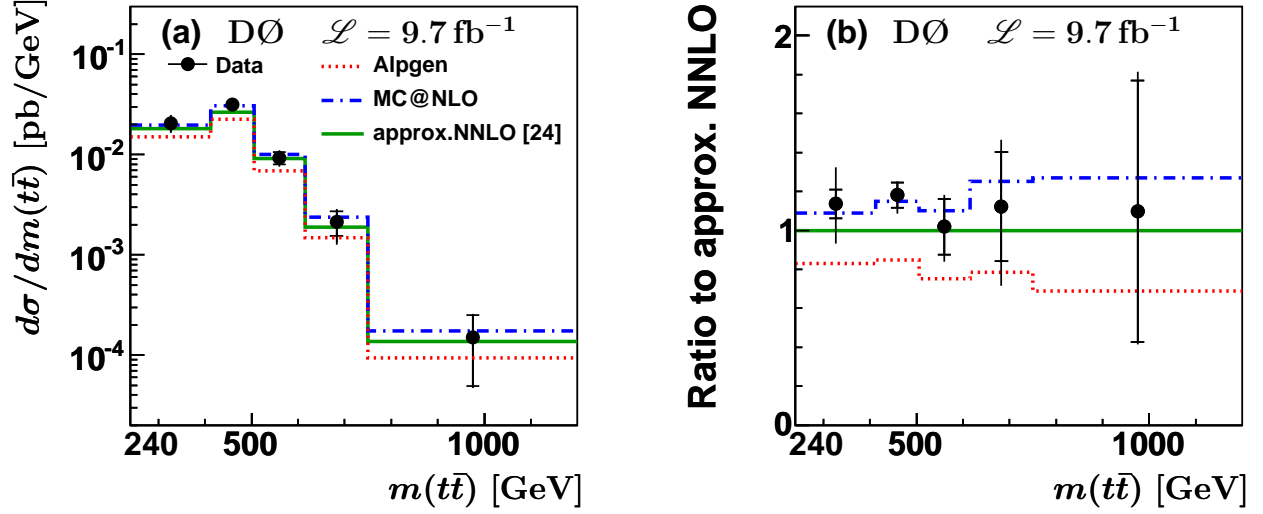


FIG. 9: (color online) (a) Measured differential cross section as a function of $m(t\bar{t})$ for data compared to several QCD predictions. The inner error bars correspond to the statistical uncertainties and the outer error bars to the total uncertainties. (b) Ratio of data, ALPGEN (dashed line) and MC@NLO cross sections (dash-dotted line) to the QCD prediction at approximate NNLO [24]. MC simulations and pQCD predictions use a top quark mass of 172.5 GeV unless indicated to the contrary. Note that the correlated overall normalization uncertainty on the differential data points is about $\pm 6.6\%$.

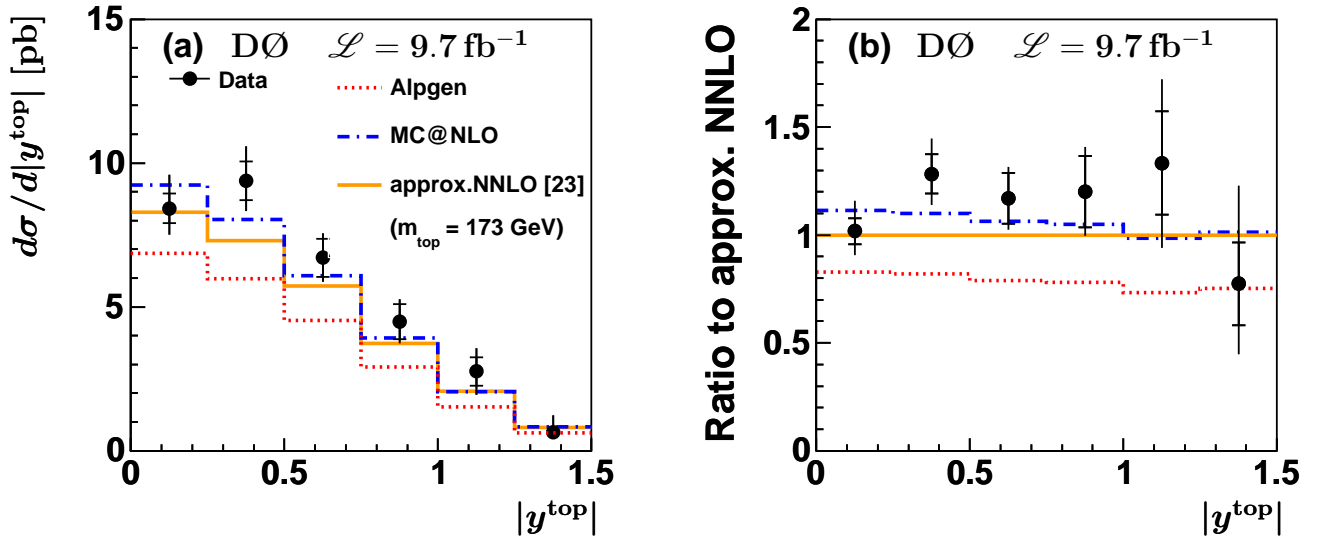


FIG. 10: (color online) (a) Measured differential cross section as a function of $|y^{\text{top}}|$ for data compared to several QCD predictions. The inner error bars correspond to the statistical uncertainties and the outer error bars to the total uncertainties. (b) Ratio of data, ALPGEN (dashed line) and MC@NLO cross sections (dash-dotted line) to the QCD prediction at approximate NNLO [23]. MC simulations and pQCD predictions use a top quark mass of 172.5 GeV unless indicated to the contrary. Note that the correlated overall normalization uncertainty on the differential data points is about $\pm 6.6\%$.

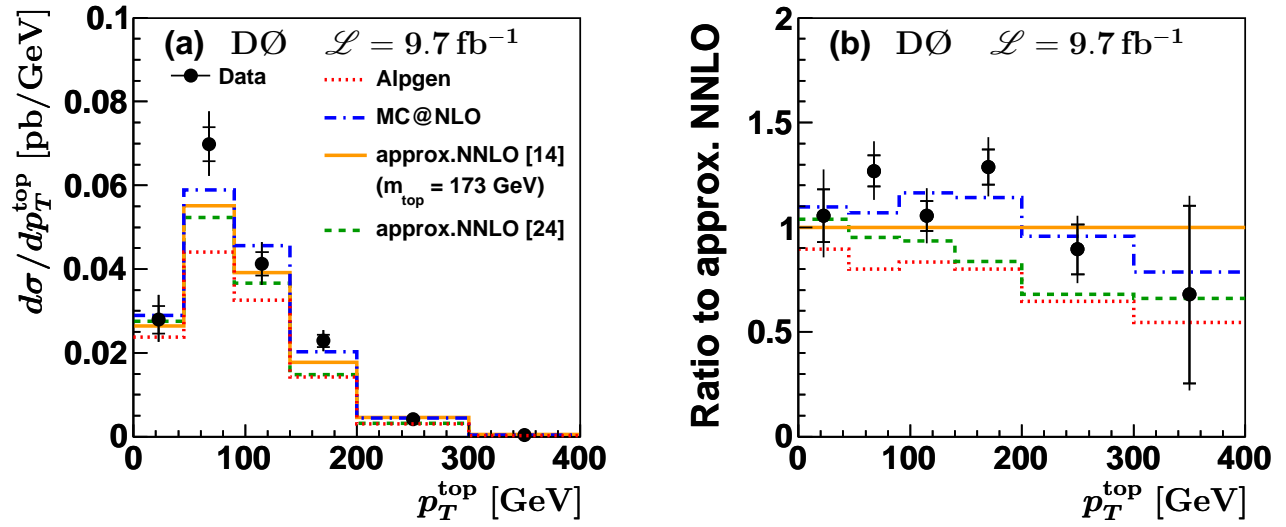


FIG. 11: (color online) (a) Measured differential cross section as a function of p_T^{top} for data compared to several QCD predictions. The inner error bars correspond to the statistical uncertainties and the outer error bars to the total uncertainties. (b) Ratio of data, ALPGEN (dashed line) and MC@NLO cross sections (dash-dotted line) to the QCD prediction at approximate NNLO [14]. MC simulations and pQCD predictions use a top quark mass of 172.5 GeV unless indicated to the contrary. Note that the correlated overall normalization uncertainty on the differential data points is about $\pm 6.6\%$.

We would like to thank W. Bernreuther and Z. G. Si for useful discussions on differential top quark cross sections. We thank the staffs at Fermilab and collaborating institutions, and acknowledge support from the Department of Energy and National Science Foundation (United States of America); Alternative Energies and Atomic Energy Commission and National Center for Scientific Research/National Institute of Nuclear and Particle Physics (France); Ministry of Education and Science of the Russian Federation, National Research Center “Kurchatov Institute” of the Russian Federation, and Russian Foundation for Basic Research (Russia); National Council for the Development of Science and Technology and Carlos Chagas Filho Foundation for the Support of Research in the State of Rio de Janeiro (Brazil); Department of Atomic Energy and Department of Science and Tech-

nology (India); Administrative Department of Science, Technology and Innovation (Colombia); National Council of Science and Technology (Mexico); National Research Foundation of Korea (Korea); Foundation for Fundamental Research on Matter (The Netherlands); Science and Technology Facilities Council and The Royal Society (United Kingdom); Ministry of Education, Youth and Sports (Czech Republic); Bundesministerium für Bildung und Forschung (Federal Ministry of Education and Research) and Deutsche Forschungsgemeinschaft (German Research Foundation) (Germany); Science Foundation Ireland (Ireland); Swedish Research Council (Sweden); China Academy of Sciences and National Natural Science Foundation of China (China); and Ministry of Education and Science of Ukraine (Ukraine).

-
- [1] CDF Collaboration, F. Abe *et al.*, Phys. Rev. Lett. **74**, 2626 (1995).
 - [2] D0 Collaboration, S. Abachi *et al.*, Phys. Rev. Lett. **74**, 2632 (1995).
 - [3] CDF & D0 Collaboration, V. M. Abazov *et al.*, Phys. Rev. D **86**, 092003 (2012).
 - [4] D0 Collaboration, V. M. Abazov *et al.*, Phys. Rev. D **84**, 112005 (2011).
 - [5] CDF Collaboration, T. Aaltonen *et al.*, Phys. Rev. D **87**, 092002 (2013).
 - [6] D0 Collaboration, V. M. Abazov *et al.*, Phys. Rev. D **88**, 112002 (2013).
 - [7] CDF Collaboration, T. Aaltonen *et al.*, Phys. Rev. D **88**, 072003 (2013).
 - [8] L. J. Hall and A. E. Nelson, Phys. Lett. B **153**, 430 (1985).
 - [9] P. H. Frampton and S. L. Glashow, Phys. Lett. B **190**, 157 (1987).
 - [10] CDF Collaboration, T. Aaltonen *et al.*, Phys. Rev. Lett. **102**, 222003 (2009).
 - [11] D0 Collaboration, V. M. Abazov *et al.*, Phys. Lett. B **693**, 515 (2010).
 - [12] CMS Collaboration, S. Chatrchyan *et al.*, Eur. Phys. J. C **73**, 2339 (2013).
 - [13] ATLAS Collaboration, G. Aad *et al.*, Eur. Phys. J. C **73**, 2261 (2013).
 - [14] N. Kidonakis, Phys. Rev. D **82**, 114030 (2010).
 - [15] R. Brun and F. Carminati, CERN Program Library Long Writeup W5013 (1993) (unpublished).
 - [16] S. Frixione and B. R. Webber, J. High Energy Phys. 06 (2002) 029; S. Frixione *et al.*, J. High Energy Phys. 08 (2003) 007.
 - [17] M. L. Mangano *et al.*, J. High Energy Phys. 07 (2003) 001.
 - [18] E. E. Boos, V. E. Bunichev *et al.*, Physics of Atomic Nuclei, 780 (2006).
 - [19] G. Corcella *et al.*, J. High Energy Phys. 01 (2001) 010.
 - [20] T. Sjöstrand, S. Mrenna, and P. Skands, J. High Energy Phys. 05 (2006) 026.
 - [21] J. Pumplin *et al.*, J. High Energy Phys. 07 (2002) 12.
 - [22] J. Pumplin *et al.*, J. High Energy Phys. 10 (2003) 46.
 - [23] N. Kidonakis, Phys. Rev. D **84**, 011504(R) (2011).
 - [24] V. Ahrens *et al.*, J. High Energy Phys. 09 (2010) 097.
 - [25] A. D. Martin, W. J. Stirling, R. S. Thorne and G. Watt, Eur. Phys. J. C **63**, 189 (2009).
 - [26] P. Barnreuther, M. Czakon and A. Mitov, Phys. Rev. Lett. **109** 132001 (2012).
 - [27] J. Campell, R. K. Ellis, Nucl. Phys. Proc. Suppl. **10** 205 (2010).
 - [28] D0 Collaboration, V. M. Abazov *et al.*, Phys. Lett. B **693**, 522 (2010).
 - [29] C. Balazs and C. P. Yuan, Phys. Rev. D **56**, 5558 (1997).
 - [30] N. Kidonakis, Phys. Rev. D **74**, 114012 (2006).
 - [31] D0 Collaboration, V. M. Abazov *et al.*, Nucl. Instrum. Methods Sect. A **565**, 463 (2006).
 - [32] S. N. Ahmed *et al.*, Nucl. Instrum. Methods Sect. A **634**, 8 (2011).
 - [33] R. Angstadt *et al.*, Nucl. Instrum. Methods Sect. A **622**, 298 (2010).
 - [34] D0 Collaboration, V. M. Abazov *et al.*, Nucl. Instrum. Methods Sect. A **763**, 290 (2014).
 - [35] T. Andeen *et al.*, FERMILAB-TM-2365 (2007).
 - [36] D0 Collaboration, V. M. Abazov *et al.*, Nucl. Instrum. Methods Sect. A **737**, 281 (2014).
 - [37] D0 Collaboration, V. M. Abazov *et al.*, Nucl. Instrum. Methods Sect. A **750**, 78 (2014).
 - [38] D0 Collaboration, V. M. Abazov *et al.*, Phys. Rev. Lett. **101**, 062001 (2008).
 - [39] D0 Collaboration, V. M. Abazov *et al.*, Phys. Rev. D **74**, 112004 (2006).
 - [40] D0 Collaboration, V. M. Abazov *et al.*, Phys. Rev. D **84**, 012008 (2011).
 - [41] D. L. Phillips, J. Assoc. Comp. Mach. **9** **84** (1962).
 - [42] A. N. Tikhonov, Soviet Math. Dokl. **4** 1035 (1963).
 - [43] V. Blobel, Proc. Advanced Statistical Techniques in Particle Physics, Durham (2002).
 - [44] E. H. Moore, Bulletin of the American Mathematical Society **26** (9) 394395 (1920).
 - [45] R. Brun and F. Rademakers, Nucl. Instrum. Methods Sect. A **389**, 81 (1997); S. Schmitt, J. of Instrumentation **7**, T10003 (2012).
 - [46] S. Snyder, Doctoral Thesis, State University of New York at Stony Brook (1995).
 - [47] J. Beringer *et al.* (Particle Data Group), Phys. Rev. D

- 86**, 010001 (2012).
- [48] D0 Collaboration, V. M. Abazov *et al.*, Phys. Rev. D **84**, 032004 (2011).
- [49] D. Meister, Master thesis (<http://e-collection.library.ethz.ch/eserv/eth:6999/eth-6999-01.pdf>), University of Illinois Chicago (visitor from ETH-Zürich) (2012).
- [50] A. Hoecker and V. Kartvelishvili, Nucl. Instrum. Methods in Phys. Res. A **372**, 469 (1996).

Appendix A: Cross section tables and covariance matrices

The correlation coefficients for the differential cross sections are given in Table IV, V, and VI, which are

helpful in interpreting the differential cross sections as shown in Figs. 9, 10, and 11. The numerical values of the cross sections are given as a function of $m(t\bar{t})$, $|y^{\text{top}}|$, and p_T^{top} in Table VII, VIII, and IX, respectively. Contributions beyond the highest bin boundary are included in the last bin of the $m(t\bar{t})$, $|y^{\text{top}}|$ and p_T^{top} table entries. The full covariance matrices for these cross sections are given in Table X, XI, and XII. The results of diagonalizing the covariance matrices in terms of eigenvalues and corresponding eigenvectors are presented in Tables XIII, XIV, and XV.

TABLE IV: Correlation coefficients of the differential cross section as a function of $m(t\bar{t})$.

$m(t\bar{t})$ [TeV]	0.2400 – 0.4125	0.4125 – 0.5050	0.5050 – 0.6150	0.6150 – 0.7500	0.7500 – 1.200
0.2400 – 0.4125	1	−0.45	+0.13	−0.02	−0.00
0.4125 – 0.5050	−0.45	1	−0.51	+0.12	+0.01
0.5050 – 0.6150	+0.13	−0.51	1	−0.48	+0.02
0.6150 – 0.7500	−0.02	+0.12	−0.48	1	−0.63
0.7500 – 1.2000	−0.00	+0.01	+0.02	−0.63	1

TABLE V: Correlation coefficients of the differential cross section as a function of $|y^{\text{top}}|$.

$ y^{\text{top}} $	0.00 – 0.25	0.25 – 0.50	0.50 – 0.75	0.75 – 1.00	1.00 – 1.25	1.25 – 1.50
0.00 – 0.25	1	−0.51	−0.06	−0.02	−0.01	−0.00
0.25 – 0.50	−0.51	1	−0.39	−0.02	−0.01	−0.01
0.50 – 0.75	−0.06	−0.39	1	−0.41	−0.00	−0.00
0.75 – 1.00	−0.02	−0.02	−0.41	1	−0.41	−0.01
1.00 – 1.25	−0.01	−0.01	−0.00	−0.41	1	−0.46
1.25 – 1.50	−0.00	−0.01	−0.00	−0.01	−0.46	1

TABLE VI: Correlation coefficients of the differential cross section as a function of p_T^{top} .

p_T^{top} [TeV]	0.000 – 0.045	0.045 – 0.090	0.090 – 0.140	0.140 – 0.200	0.200 – 0.300	0.300 – 0.500
0.000 – 0.045	1	−0.55	+0.01	+0.00	−0.00	−0.00
0.045 – 0.090	−0.55	1	−0.42	+0.02	+0.00	−0.00
0.090 – 0.140	+0.01	−0.42	1	−0.37	−0.01	−0.00
0.140 – 0.200	+0.00	+0.02	−0.37	1	−0.29	−0.03
0.200 – 0.300	−0.00	+0.00	−0.01	−0.29	1	−0.15
0.300 – 0.500	−0.00	+0.00	−0.00	−0.03	−0.15	1

TABLE VII: Average value of $m(t\bar{t})$ and differential cross section in each bin of $m(t\bar{t})$. In addition to the systematic uncertainty reported in column five there is a 6.1% normalization uncertainty across all bins due to the uncertainty on the integrated luminosity.

$m(t\bar{t})$ [TeV]	$\langle M(t\bar{t}) \rangle$ [TeV]	$d\sigma/dM(t\bar{t})$ [pb/TeV]	$\delta^{\text{stat.}}$ [pb/TeV]	$\delta^{\text{sys.}}$ [pb/TeV]
0.2400 – 0.4125	0.36	20.60	± 1.52	+3.86 −3.76
0.4125 – 0.5050	0.46	31.26	± 2.03	+1.84 −2.20
0.5050 – 0.6150	0.55	9.38	± 1.34	+0.78 −1.00
0.6150 – 0.7500	0.67	2.13	± 0.59	+0.43 −0.63
0.7500 – 1.2000	0.83	0.15	± 0.10	+0.06 −0.05

TABLE VIII: Average value of $|y^{\text{top}}|$ and differential cross section in each bin of $|y^{\text{top}}|$. In addition to the systematic uncertainty reported in column five there is a 6.1% normalization uncertainty across all bins due to the uncertainty on the integrated luminosity.

$ y^{\text{top}} $	$\langle y (t/\bar{t}) \rangle$	$d\sigma/d y (t/\bar{t})$ [pb]	$\delta^{\text{stat.}}$ [pb]	$\delta^{\text{sys.}}$ [pb]
0.00 – 0.25	0.13	8.50	± 0.51	+0.67 −0.99
0.25 – 0.50	0.37	9.46	± 0.67	+0.63 −0.88
0.50 – 0.75	0.62	6.72	± 0.67	+0.29 −0.30
0.75 – 1.00	0.86	4.64	± 0.64	+0.36 −0.41
1.00 – 1.25	1.11	2.73	± 0.49	+0.66 −0.63
1.25 – 1.50	1.36	0.63	± 0.16	+0.25 −0.25

TABLE IX: Average value of p_T^{top} and differential cross section in each bin of p_T^{top} . In addition to the systematic uncertainty reported in column five there is a 6.1% normalization uncertainty across all bins due to the uncertainty on the integrated luminosity.

p_T^{top} [TeV]	$\langle p_T(t/\bar{t}) \rangle$ [TeV]	$d\sigma/dp_T(t/\bar{t})$ [pb/TeV]	$\delta^{\text{stat.}}$ [pb/TeV]	$\delta^{\text{sys.}}$ [pb/TeV]
0.000 – 0.045	0.030	27.76	± 3.31	$+3.21$ -4.29
0.045 – 0.090	0.068	69.70	± 4.07	$+1.79$ -2.88
0.090 – 0.140	0.112	41.47	± 2.78	$+3.34$ -3.45
0.140 – 0.200	0.164	22.84	± 1.51	$+1.25$ -1.34
0.200 – 0.300	0.234	4.18	± 0.56	$+0.41$ -0.39
0.300 – 0.500	0.321	0.32	± 0.20	$+0.07$ -0.09

TABLE X: Covariance matrix (statistical and systematical uncertainties) of the differential cross section as a function of $m(t\bar{t})$. The systematic uncertainty is assumed to be 100% correlated.

$m(t\bar{t})$ [TeV]	0.2400 – 0.4125	0.4125 – 0.5050	0.5050 – 0.6150	0.6150 – 0.7500	0.7500 – 1.200
0.2400 – 0.4125	+16.832	–1.430	+0.364	–0.051	–0.001
0.4125 – 0.5050	–1.430	+6.436	–1.820	+0.321	+0.021
0.5050 – 0.6150	+0.364	–1.820	+2.570	–0.635	+0.020
0.6150 – 0.7500	–0.051	+0.321	–0.635	+0.633	–0.141
0.7500 – 1.2000	–0.001	+0.021	+0.020	–0.141	+0.129

TABLE XI: Covariance matrix (statistical and systematical uncertainties) of the differential cross section as a function of $|y^{\text{top}}|$. The systematic uncertainty is assumed to be 100% correlated.

$ y^{\text{top}} $	0.00 – 0.25	0.25 – 0.50	0.50 – 0.75	0.75 – 1.00	1.00 – 1.25	1.25 – 1.50
0.00 – 0.25	+0.952	–0.164	–0.017	–0.004	–0.001	–0.000
0.25 – 0.50	–0.164	+1.029	–0.163	–0.008	–0.001	–0.001
0.50 – 0.75	–0.017	–0.163	+0.551	–0.155	–0.001	–0.000
0.75 – 1.00	–0.004	–0.008	–0.155	+0.557	–0.121	–0.002
1.00 – 1.25	–0.001	–0.001	–0.001	–0.121	+0.609	–0.062
1.25 – 1.50	–0.000	–0.001	–0.000	–0.002	–0.062	+0.087

TABLE XII: Covariance matrix (statistical and systematical uncertainties) of the differential cross section as a function of p_T^{top} . The systematic uncertainty is assumed to be 100% correlated.

p_T^{top} [TeV]	0.000 – 0.045	0.045 – 0.090	0.090 – 0.140	0.140 – 0.200	0.200 – 0.300	0.300 – 0.500
0.000 – 0.045	+25.018	–8.692	+0.157	+0.011	–0.008	–0.000
0.045 – 0.090	–8.692	+22.028	–5.916	+0.155	+0.0149	+0.000
0.090 – 0.140	+0.157	–5.916	+19.277	–1.958	–0.037	–0.001
0.140 – 0.200	+0.011	+0.155	–1.958	+3.942	–0.324	–0.009
0.200 – 0.300	–0.008	+0.015	–0.037	–0.324	+0.469	–0.013
0.300 – 0.500	–0.000	+0.000	–0.001	–0.009	–0.013	+0.047

TABLE XIII: Eigenvalues and eigenvectors of the covariance matrix (see Table X) of the differential cross section as a function of $m(t\bar{t})$. The contribution of the eigenvector is listed in the first column together with its error calculated as the square root of the eigenvalue λ . The eigenvalue λ in the second column followed by the elements of the eigenvectors in bins of $m(t\bar{t})$.

Contribution [pb/TeV]	λ	$m(t\bar{t})$ range [TeV]				
		0.2400 – 0.4125	0.4125 – 0.5050	0.5050 – 0.6150	0.6150 – 0.7500	0.7500 – 1.2000
1.655 ± 0.284	0.081	–0.000	+0.003	+0.079	+0.330	+0.941
6.361 ± 0.691	0.478	+0.000	+0.050	+0.316	+0.886	–0.337
19.747 ± 1.416	2.004	+0.015	+0.383	+0.867	–0.316	+0.037
28.166 ± 2.643	6.985	+0.147	+0.911	–0.375	+0.082	+0.000
16.360 ± 4.129	17.052	+0.989	–0.141	+0.043	–0.007	–0.000

TABLE XIV: Eigenvalues and eigenvectors of the covariance matrix (see Table XI) of the differential cross section as a function of $|y^{\text{top}}|$. The contribution of the eigenvector is listed in the first column together with its error calculated as the square root of the eigenvalue λ . The eigenvalue λ in the second column followed by the elements of the eigenvectors in bins of $|y^{\text{top}}|$.

Contribution [pb]	λ	$ y^{\text{top}} $ range					
		0.00 – 0.25	0.25 – 0.50	0.50 – 0.75	0.75 – 1.00	1.00 – 1.25	1.25 – 1.50
0.387 ± 0.283	0.080	−0.000	+0.001	−0.010	+0.027	−0.111	+0.993
0.934 ± 0.590	0.348	+0.029	−0.164	+0.685	−0.662	+0.248	+0.053
2.496 ± 0.763	0.582	+0.080	−0.249	+0.587	+0.430	−0.630	−0.076
5.194 ± 0.872	0.761	+0.200	−0.273	+0.214	+0.570	+0.715	+0.067
0.864 ± 0.922	0.851	−0.800	+0.455	+0.297	+0.212	+0.138	+0.012
14.188 ± 1.092	1.192	+0.559	+0.794	+0.229	+0.073	+0.020	+0.002

TABLE XV: Eigenvalues and eigenvectors of the covariance matrix (see Table XII) of the differential cross section as a function of p_T^{top} . The contribution of the eigenvector is listed in the first column together with its error calculated as the square root of the eigenvalue λ . The eigenvalue λ in the second column followed by the elements of the eigenvectors in bins of p_T^{top} .

Contribution [pb/TeV]	λ	p_T^{top} range [TeV]					
		0.000 – 0.045	0.045 – 0.090	0.090 – 0.140	0.140 – 0.200	0.200 – 0.300	0.300 – 0.500
0.648 ± 0.214	0.046	+0.000	+0.000	+0.001	+0.006	+0.036	+0.999
7.162 ± 0.661	0.437	+0.001	+0.003	+0.013	+0.099	+0.994	−0.037
31.477 ± 1.924	3.703	+0.017	+0.045	+0.140	+0.984	−0.100	−0.002
81.156 ± 3.451	11.906	+0.461	+0.705	+0.526	−0.115	+0.002	+0.000
1.400 ± 4.601	21.160	+0.561	+0.235	−0.788	+0.092	−0.000	+0.000
16.028 ± 5.790	33.529	−0.687	+0.667	−0.288	+0.022	+0.001	+0.000